



**HAL**  
open science

## Chemical and boron isotope composition of tourmaline from the Kiaka orogenic gold deposit (Burkina Faso, West African Craton) as a proxy for ore-forming processes

J. Gauriau, M. Harlaux, Anne-Sylvie André-Mayer, A. Eglinger, A. Richard, A. Fontaine, M.G. Lefebvre, D. Béziat, J. Villeneuve, D. Lemarchand

### ► To cite this version:

J. Gauriau, M. Harlaux, Anne-Sylvie André-Mayer, A. Eglinger, A. Richard, et al.. Chemical and boron isotope composition of tourmaline from the Kiaka orogenic gold deposit (Burkina Faso, West African Craton) as a proxy for ore-forming processes. *Mineralium Deposita*, 2020, 10.1007/s00126-020-01002-7. hal-02958894

**HAL Id: hal-02958894**

**<https://hal.univ-lorraine.fr/hal-02958894v1>**

Submitted on 12 Oct 2020

**HAL** is a multi-disciplinary open access archive for the deposit and dissemination of scientific research documents, whether they are published or not. The documents may come from teaching and research institutions in France or abroad, or from public or private research centers.

L'archive ouverte pluridisciplinaire **HAL**, est destinée au dépôt et à la diffusion de documents scientifiques de niveau recherche, publiés ou non, émanant des établissements d'enseignement et de recherche français ou étrangers, des laboratoires publics ou privés.

1 Chemical and boron isotope composition of tourmaline from the Kiaka  
2 orogenic gold deposit (Burkina Faso, West African Craton) as a proxy  
3 for ore-forming processes

4

5 J. Gauriau <sup>1,2\*</sup>, M. Harlaux <sup>3</sup>, A.-S. André-Mayer <sup>1\*</sup>, A. Eglinger <sup>1</sup>, A. Richard <sup>1</sup>, A. Fontaine <sup>4</sup>,  
6 M.G. Lefebvre <sup>5</sup>, D. Béziat <sup>6</sup>, J. Villeneuve <sup>7</sup>, D. Lemarchand <sup>8</sup>

7

8 <sup>1</sup> Université de Lorraine, CNRS, GeoRessources, F-54000 Nancy, France

9 <sup>2</sup> Present address: Department of Earth Sciences, University of Southern California, Los  
10 Angeles, CA 90089-0740, USA

11 <sup>3</sup> Nevada Bureau of Mines and Geology, University of Nevada, Reno, NV 89557-0178, USA

12 <sup>4</sup> Institut National de la Recherche Scientifique (INRS), 490 rue de la couronne, G1K 9A9,  
13 Quebec City, QC, Canada

14 <sup>5</sup> GFZ German Research Centre for Geosciences, Telegrafenberg, 14473 Potsdam, Germany

15 <sup>6</sup> Géosciences Environnement Toulouse (GET), Université Paul Sabatier, CNRS, IRD, 14  
16 Avenue Edouard Belin, 31400 Toulouse, France

17 <sup>7</sup> Centre de Recherches Pétrographiques et Géochimiques (CRPG), CNRS-Université de  
18 Lorraine, 15 rue Notre-Dame des Pauvres, 54501 Vandœuvre-lès Nancy, France

19 <sup>8</sup> Laboratoire d'Hydrologie et de Géochimie de Strasbourg (LHYGES), Université de  
20 Strasbourg-EOST, CNRS, ENGEES, 1 rue Blessig, 67084 Strasbourg Cedex, France

21

22 \* Corresponding authors: anne-sylvie.andre@univ-lorraine.fr, gauriau@usc.edu

23

24 **Abstract**

25 The Kiaka orogenic gold deposit (Burkina Faso), located in the Paleoproterozoic domain of the  
26 West African Craton, is characterized by a two-stage gold mineralization hosted in volcano-  
27 sedimentary metamorphic rocks that was formed during the Eoeburnean (2.20-2.13 Ga) and  
28 Eburnean (2.13-2.05 Ga) orogenic cycles. These two stages include an early disseminated low-  
29 grade gold mineralization and a late vein-hosted high-grade gold mineralization. A paragenetic  
30 study indicates that the first gold stage was coeval with the deposition of hydrothermal  
31 tourmaline. The aim of this paper is twofold: (i) to determine the processes responsible for the  
32 economic disseminated gold mineralization, and (ii) to identify the source of the mineralizing  
33 fluids. To this end, we combine *in situ* analyses obtained from electron probe microanalysis and  
34 secondary ion mass spectrometry measurements. A dravite composition characterizes the  
35 hydrothermal tourmaline hosted in metamafic volcanic rocks and metagreywackes, and  $\delta^{11}\text{B}$   
36 values range within the two intervals [-25.1‰; -22.0‰] and [-19.6‰; -15.1‰]. Our results  
37 suggest that tourmaline formed from a high-temperature (ca. 400°C), reduced, and low-salinity  
38 hydrothermal fluid that interacted with the local host rocks. From the modeling of tourmaline-  
39 fluid boron isotope fractionation, we infer a metamorphic fluid origin derived from  
40 devolatilization of deeply-buried muscovite schists during the regional prograde to peak  
41 metamorphism prior ca. 2.13 Ga. This metamorphic fluid-rock interaction model may possibly  
42 extend to other orogenic gold deposits in the West African Craton.

43 **Keywords**

44 Tourmaline, Boron isotopes, Orogenic gold deposit, West African Craton, Burkina Faso.

## 45 INTRODUCTION

46

47 Tourmaline is the most important borosilicate mineral on Earth and represents a reliable  
48 monitor of the physico-chemical conditions of the environment in which it crystallized due to  
49 three main properties: (i) it is a stable mineral over a large range of pressure and temperature  
50 conditions, (ii) it has a complex crystal chemistry incorporating a large range of chemical  
51 elements, and (iii) it shows negligible intracrystalline diffusion, making it an excellent  
52 petrogenetic indicator for determining fluid sources and processes (Dutrow and Henry 2011;  
53 Slack and Trumbull 2011; van Hinsberg et al. 2011). Tourmaline is a common mineral in  
54 orogenic gold deposits worldwide, often found disseminated in gold-bearing quartz veins or as  
55 metasomatic replacements along the host rock vein selvages. Deposition of tourmaline and gold  
56 is generally interpreted to be synchronous (King and Kerrich 1989; Mueller et al. 1991; Kotzer  
57 et al. 1993; Anglin et al. 1996; Frei and Pettke 1996; Slack 1996; Rowins et al. 1997; Jiang  
58 1998; Béziat et al. 1999), suggesting that tourmaline can be used as a proxy for tracing the ore-  
59 forming processes.

60 Fluid and metal sources in orogenic gold deposits, including Au and B, are still debated,  
61 therefore a large diversity of genetic models have been proposed. This diversity may either  
62 reflect an intrinsic variability of orogenic gold deposits or may show divergence between  
63 interpretations. The current paradigm for the formation of orogenic gold deposits involves a  
64 metamorphic fluid derived from devolatilization of thick metasedimentary sequences during  
65 prograde to retrograde metamorphic evolution of greenstone belts (e.g. Wyman and Kerrich  
66 1988; Goldfarb et al. 2005; Phillips and Powell 2010; Goldfarb and Groves 2015; Fusswinkel  
67 et al. 2017; Groves et al. 2019). Alternatively, a magmatic origin for fluids and metals related  
68 to reduced intrusions has been proposed (Burrows and Spooner 1987; Wang et al. 1993;  
69 Tomkins 2013; Xue et al. 2013), as well as mixed magmatic-metamorphic fluid origins (Rogers

70 et al. 2013; Molnár et al. 2016). The source of boron in orogenic gold environments may be  
71 derived from (i) metamorphic fluids produced during devolatilization reactions of  
72 metasedimentary sequences that occur above 650°C (Spear et al. 1999; van Hinsberg et al.  
73 2011), and/or (ii) magmatic fluids released from boron-rich reduced magmas (Trumbull and  
74 Slack 2018). In previous studies, tourmaline has been used as a proxy for (i) to identify trace  
75 elements that discriminate tourmaline from gold-bearing veins from orogenic gold deposits  
76 (Sciuba et al. 2020), (ii) tracing the origin of hydrothermal fluids and metals (distal vs.  
77 proximal; metamorphic vs. magmatic) and for (iii) determining the ore-forming processes  
78 yielding to deposition of gold, such as in the Yilgarn craton (Jiang et al. 2002), the Archean  
79 Abitibi belt (King and Kerrich 1989; Beaudoin et al. 2013), the Archean Barberton greenstone  
80 belt (Byerly and Palmer 1991), the Archean Hattu schist belt (Molnár et al. 2016), the Hutti-  
81 Maski Greenstone Belt (Hazarika et al. 2015), and the Paleoproterozoic West African Craton  
82 (Lambert-Smith et al. 2016; this study).

83 The Kiaka orogenic gold deposit (Burkina Faso) is hosted in the Manga Fada N’Gourma  
84 Paleoproterozoic greenstone belt, located on the southeast domain of the West African Craton.  
85 The regional host rocks consist of metavolcanic and metasedimentary units composed of  
86 metapelites, greywackes, and schists. A dioritic pluton dated at  $2140 \pm 7$  Ma (Fontaine et al.  
87 2017) intruded the schists contemporaneously with a regional shearing event. The Kiaka deposit  
88 contains a polyphase gold mineralization formed between ca. 2150 Ma and 2080 Ma that is  
89 interpreted to be coeval with the deposition of hydrothermal tourmaline (Fontaine et al. 2017;  
90 Le Mignot et al. 2017). This paper provides new data on the chemical and boron isotopic  
91 composition of hydrothermal tourmaline, as well as whole-rock boron isotope composition of  
92 the host rocks. The objective is to trace the ore-forming processes and the origin of mineralizing  
93 fluids in the Kiaka gold deposit, focusing specifically on hydrothermal tourmaline associated  
94 to the ca. 2150 Ma disseminated gold mineralization. The origin of the mineralizing fluids is

95 discussed relative to the two potential sources: the dioritic intrusion (magmatic origin) and the  
96 metasedimentary rocks (metamorphic origin).

97

## 98 **GEOLOGICAL CONTEXT**

99

### 100 **The Paleoproterozoic Baoulé-Mossi domain**

101 The Paleoproterozoic southern part of the West African Craton (WAC) is composed of low-  
102 grade volcanic and volcano-sedimentary Birimian rocks (ca. 2.20-2.14 Ga) and siliciclastic  
103 sediments (ca. 2.13-2.09 Ga) that were intruded by voluminous granites (Grenholm et al. 2019).  
104 The oldest Birimian sequence consists of tholeiitic basalt, gabbro, pyroxenite, and minor calc-  
105 alkaline ultramafic-mafic to differentiated suites (Baratoux et al. 2011). The geodynamic  
106 context of formation of the Birimian rocks remains unclear and several interpretations have  
107 been proposed, including a plume-related oceanic plateau (Abouchami et al. 1990; Boher et al.  
108 1992; Augustin and Gaboury 2017) and an oceanic context evolving from a MORB-like domain  
109 to an increasingly mature volcanic arc domain (Pouclet et al. 2006; Baratoux et al. 2011; Labou  
110 et al. 2020). This period characterizes the Eoeburnean cycle, defined by an early magmatic  
111 accretion stage followed by an arc construction stage in a convergent setting (Baratoux et al.  
112 2011; McFarlane et al. 2019). The Eburnean orogenic cycle started with the filling of major  
113 sedimentary basins by flysch sequences derived from the erosion of the Birimian crust and their  
114 inversion between ca. 2.13 Ga and 2.10 Ga (Davis et al. 2015; Grenholm et al. 2019). Different  
115 depositional settings have been proposed such as syn-orogenic foreland basin sedimentation  
116 (Feybesse et al. 2006; Block et al. 2016) or back-arc and fore-arc basin sedimentation controlled  
117 by extensional detachments (Perrouy et al. 2012; Grenholm et al. 2019). The paroxysm of the  
118 Eburnean cycle is characterized by tectonic accretion and crustal reworking between ca. 2.09  
119 and 2.05 Ga (e.g. Masurel et al. submitted). Large transpressional shear zones cross-cut the

120 Baoulé-Mossi domain contemporaneously with the emplacement of high-K calc-alkaline to  
121 shoshonitic granitic plutons (Feybesse and Milési 1994; Egal et al. 2002; Parra-Avila et al.  
122 2019) in syn- to post-collisional settings (Eglinger et al. 2017; Masurel et al. 2017; Thébaud et  
123 al. 2020).

124

### 125 **Paleoproterozoic gold metallogeny of the Baoulé-Mossi domain**

126 West Africa is currently the largest Paleoproterozoic gold-producing region in the world with  
127 an annual gold production of ca. 250 t (Béziat et al. 2008; Markwitz et al. 2016; Robertson and  
128 Peters 2016; Goldfarb et al. 2017). The majority of gold deposits are closely located to major  
129 first-order tectonic structures such as the Markoye shear zone (MSZ, Fig. 1A) in Burkina Faso  
130 (Tshibubudze and Hein 2013), the Ashanti shear zone (AS, Fig. 1A) in Ghana (Perrouty et al.  
131 2012) and the Senegal-Mali shear zone (Ledru et al. 1991, Lawrence et al. 2013) that affected  
132 greenstone belts. Gold deposits in the southern WAC formed during the long-lived period of a  
133 magmatic accretion stage, defined as the Eoeburnean cycle, and broadly during the reworking  
134 and tectonic accretion stages of the Eburnean orogenic cycle (Masurel et al. submitted). Few  
135 absolute, and some relative ages constrain gold mineralization between ca. 2.18 and 2.06 Ga,  
136 and a few are linked to polyphase mineralization processes (such as the Obuasi Au deposit;  
137 Fougrouse et al. 2017; Le Mignot et al. 2017; Augustin et al. 2017). The oldest orogenic gold  
138 deposits are mostly known in the eastern part of the Baoulé-Mossi domain, formed during the  
139 Eoeburnean deformation between ca. 2.14 and 2.13 Ga (Lawrence et al. 2017; Le Mignot et al.  
140 2017). They include the ~5.8 Moz Kiaka gold deposit, hosted by volcano-sedimentary rocks  
141 which were deformed and metamorphosed under amphibolite facies conditions (Fontaine et al.  
142 2017). Early Eburnean gold deposits (ca. 2.11-2.09 Ga) correspond to different types of gold  
143 deposits including orogenic (Obuasi deposit; Fougrouse et al. 2017), conglomerate-hosted  
144 paleo-placer (Tarkwa deposit; Perrouty et al. 2012), granitoid-hosted (Chirano deposit;

145 Allibone et al. 2004), intrusion-related (Morila deposit; McFarlane et al. 2011), and skarn  
146 (Tongon deposit; Lawrence et al. 2017) gold deposits. Some gold deposits formed during the  
147 late Eburnean tectono-thermal activity between ca. 2.09 and 2.05 Ga following docking of the  
148 Archean and Paleoproterozoic domains within the southern WAC, synchronous with  
149 widespread high-K and shoshonitic granites (Eglinger et al. 2017; Masurel et al. 2017).  
150 Economic gold mineralization associated with this transcurrent tectonics and crust-derived  
151 magmas are widespread in the western portion of the Baoulé-Mossi domain (Thébaud et al.  
152 2020; Masurel et al. submitted).

153

#### 154 **Local geology and structural framework of the Kiaka deposit**

155 The Kiaka orogenic gold deposit is located within an elongated volcano-sedimentary sequence  
156 known as the Manga Fada N’Gourma greenstone belt, which extends along 250 km from  
157 northeast to southwest (Hottin and Ouégrago 1976; Naba et al. 2004; Ganne et al. 2012). The  
158 deposit is located at the intersection between two major structures, the Markoye Shear Zone  
159 (MSZ) and a D2-related NE-trending shear zone (Fig. 1A-B; Fontaine et al. 2017). The volcano-  
160 sedimentary sequence hosting the Kiaka deposit forms a NE-striking corridor, strongly dipping  
161 to the northwest and commonly subparallel to the regional foliation (Fig. 1B). Host rocks  
162 consist of conglomerate, metagreywacke, and metapelite, which are intercalated with garnet-  
163 orthopyroxene schists and mafic rocks (Fontaine et al. 2017). Several magmatic rocks have  
164 been described in the Kiaka area, such as a biotite-amphibole diorite plug dated at  $2140 \pm 7$  Ma  
165 (Fontaine et al. 2017) and an unfoliated biotite granite, dated between 2120 and 2100 Ma,  
166 intruding the tonalite-trondhjemite-granodiorite (TTG) basement (Castaing et al. 2003; Vegas  
167 et al. 2008; Fontaine et al. 2017). Litho-geochemical data suggest similarities between the  
168 biotite-amphibole diorite and the Tenkodogo-Yamba batholith that is part of the TTG suite  
169 (Naba et al. 2004).



170 Deposit-scale study suggests the existence of at least three main deformation phases reported  
171 as D1<sub>Ki</sub>, D2<sub>Ki</sub>, and D3-4<sub>Ki</sub> (Fontaine et al. 2017). The two first phases (D1<sub>Ki</sub> and D2<sub>Ki</sub>) occurred  
172 under ductile conditions (P=550-650°C, T=6-8 kbars; Ganne et al. 2012; Fontaine et al. 2017),  
173 whereas the others (D3<sub>Ki</sub>-D4<sub>Ki</sub>) took place at the ductile-brittle transition (P<4 kbars, T=200-  
174 450°C; Fontaine et al. 2017; Ganne et al. 2012; Block et al. 2015). The D1<sub>Ki</sub> phase corresponds  
175 to a relic structural event marked by P1<sub>Ki</sub> folds, resulting from EW to WNW-ESE compression,  
176 which are preserved in low-strain domains between D2<sub>Ki</sub> shear zones (Fontaine et al. 2017).  
177 The S2<sub>Ki</sub> regional foliation, parallel to the isoclinal P1<sub>Ki</sub> folding, records a biotite-sillimanite-  
178 garnet-amphibole assemblage, suggesting lower to middle amphibolite facies conditions (Fig.  
179 3A).

180 At the regional scale, the NE-trending D2-related shear zones and the NS-trending MSZ are the  
181 main structures controlling the emplacement of the gold mineralization at Kiaka (Fontaine et  
182 al. 2017). These structures record dextral-reverse D1 motion and sinistral-reverse D2  
183 reactivation (Tshibubudze et al. 2009; Tshibubudze and Hein 2013). Mineralized envelopes are  
184 spatially associated with the NE-trending shear zones and some of them extend along the axial  
185 plane of P2<sub>Ki</sub> isoclinal folds (Fontaine et al. 2017). The sinistral-reverse D2 reactivation is  
186 coeval with the emplacement of the Kiaka diorite dated at  $2140 \pm 7$  Ma. The D3-4<sub>Ki</sub> phases  
187 correspond to quartz-carbonate veins that formed during reactivation along D2-related shear  
188 zones and retrogression at greenschist facies conditions (Fontaine et al. 2017), likely during or  
189 after the ductile-brittle transition.

190

### 191 **Tourmaline paragenesis and space-time relationships with gold mineralization**

192 A relative chronology between tectono-metamorphic and hydrothermal events has been  
193 proposed by Fontaine et al. (2017), based on crosscutting relationships, hydrothermal

194 assemblages, and ore mineralogy, identifying two successive stages of gold mineralization and  
195 associated hydrothermal alteration in the Kiaka deposit (Fig. 2):

196 (i) The first main stage corresponds to the early sulfide-rich disseminated gold  
197 mineralization related to the D2<sub>Ki</sub> phase, coeval with emplacement of the biotite-amphibole  
198 diorite intrusion (Fig. 2). This mineralization is volumetrically the most important (>80% of the  
199 orebodies) and constitutes most of the gold resources with average grades of 1-3 g/t. The ore  
200 assemblage consists of 50µm-1mm large anhedral pyrrhotite (60-80%) that is commonly  
201 associated with sub-millimetric (200-300 µm) pyrite (10-20%), chalcopyrite (5-10%),  
202 arsenopyrite (5-10%), and rare löllingite disseminated in sericitized metagreywacke and partly  
203 in metamafic volcanic rocks, containing a biotite-titanite-clinozoisite assemblage. Gold  
204 probably occurs as nano-inclusions hosted in, or within, the crystal lattice of pyrite,  
205 arsenopyrite, and löllingite. This stage was dated at  $2157 \pm 24$  Ma (Re-Os on pyrrhotite; Le  
206 Mignot et al. 2017; Fontaine et al. 2017).

207 (ii) The second stage is related to formation of a high-grade gold mineralization at 50-  
208 60 g/t Au hosted in hydrothermal veins and breccias that formed during the D3<sub>Ki</sub> to D4<sub>Ki</sub> phases  
209 (Fig. 2). The ore assemblage is composed of pyrrhotite, chalcopyrite, arsenopyrite, electrum,  
210 native gold (2-20 µm), and tellurobismuthite, intergrown with clinozoisite, quartz, calcite, and  
211 chlorite.

212 According to Fontaine et al. (2017) and new petrographic observations, two generations of  
213 tourmaline are observed in the Kiaka deposit. A first generation of tourmaline (*Tur<sub>1</sub>*) is locally  
214 found as rounded detrital grains (<10 µm) in quartz-biotite metagreywacke, representing <5%  
215 in volume of the host rock. *Tur<sub>1</sub>* is also found within garnet-biotite-chlorite-muscovite layers  
216 hosted in muscovite schists (Fig. 3A-B), which are affected by the S2<sub>Ki</sub> foliation and associated  
217 folds, suggesting an early formation prior, or during, the D1<sub>Ki</sub> stage. A second generation of  
218 tourmaline (*Tur<sub>2</sub>*) is found in the metagreywacke and metamafic volcanic rock (referred

219 subsequently as metamafic rocks) located close to or within the mineralized zones. This  
220 tourmaline is found as large (typically 50-500  $\mu\text{m}$ ) zoned porphyroblasts containing sulfide and  
221 silicate inclusions. It is locally oriented along the  $S_{2\text{Ki}}$  foliation. In the metagreywacke,  $Tur_2$  is  
222 intergrown with an assemblage of biotite, clinozoisite, quartz, K-feldspar and disseminated  
223 sulfides, including pyrrhotite, chalcopyrite, pyrite, and arsenopyrite (Fig. 3C-D). In the  
224 metamafic rock,  $Tur_2$  is intergrown with chlorite (Chl 1, pre- to syn- $D_{1\text{Ki}}$ ), biotite, titanite,  
225 clinozoisite, and pyrrhotite, which are characteristics of the  $D_{2\text{Ki}}$  hydrothermal assemblage.  
226 Chlorite (Chl 1) inclusions oriented along an early foliation (syn- $D_{1\text{Ki}}$ ) within the poikiloblastic  
227  $Tur_2$  porphyroblasts (Fig. 5), as well as a chlorite (Chl 2)-biotite assemblage (Fig. 3F), related  
228 to the  $D_{3\text{Ki}}$  stage and overgrown by  $Tur_2$ , constraint the formation of  $Tur_2$  within syn- to late-  
229  $D_{2\text{Ki}}$  event. The assemblage of Chl 1 and biotite is interpreted as a relic from stage  $D_{1\text{Ki}}$  that  
230 was overprinted by ore stage fluids during the  $D_{2\text{Ki}}$  event in replacement zones. In contrast, the  
231 assemblage of titanite, clinozoisite, and pyrrhotite is considered to be earlier than  $D_{3\text{Ki}}$ , because  
232 it is cut by chlorite (Chl 3)-calcite veins (Fig. 3E-F). Therefore, the second generation of  
233 tourmaline ( $Tur_2$ ) is interpreted to be of hydrothermal origin and to have formed during the  
234  $D_{2\text{Ki}}$  event, coevally with formation of the Kiaka disseminated gold mineralization. In this  
235 paper, a specific focus is given on  $Tur_2$  hosted both in metagreywacke and metamafic rocks, in  
236 order to determine the fluid sources and processes related to the formation of the first gold  
237 event, i.e. the early sulfide-rich disseminated gold mineralization related to the  $D_{2\text{Ki}}$  event.  
238 Early detrital  $Tur_1$  was not investigated because it formed before the gold mineralization and  
239 thus cannot be used as a tracer of ore-forming processes and mineralizing fluids.

240

## 241 **SAMPLE DESCRIPTION AND ANALYTICAL METHODS**

242

### 243 **Sample description**

244 Representative samples of the four main lithologies of the Kiaka deposit were collected from  
245 drill cores (spacing >400 m) intersecting the main orebody and alteration zones. Investigation  
246 of these lithologies was carried out in order to document the hydrothermal alteration by the  
247 gold-bearing fluids and to identify the presence of hydrothermal tourmaline. These lithologies  
248 include:

249 (i) Muscovite schists: they are mostly located in the southern part of the deposit in  
250 the footwall of the D2-related shear zone (Fig. 1). They represent 50 to 100 m thick lenses  
251 intercalated between metagreywacke and metavolcanic rocks. The muscovite schists contain  
252 folded tourmaline (*Tur<sub>1</sub>*)-garnet-biotite-chlorite-muscovite layers (Fig. 3A-B) and rare  
253 pyrrhotite grains. The muscovite schist sample (drill KDH75, depth 64.9 m) is located at about  
254 1-2 m from the mineralized zones and is weakly hydrothermally altered.

255 (ii) Diorite: it consists of sub-vertical intrusive plugs within the metasedimentary  
256 sequence in the northern part of the deposit (Fig. 1C). It is interpreted to be contemporaneous  
257 with the D2<sub>Ki</sub> event generating sinistral displacement along mineralized, NE-trending D2 shear  
258 zones. The diorite is dominantly composed of plagioclase, amphibole, chlorite, biotite, and  
259 quartz. No tourmaline was found in the diorite. Sample KDH337 (depth 44.1m) is located at  
260 about 50 m from the mineralized zones and is weakly hydrothermally altered, containing rare  
261 grains of pyrrhotite and chalcopyrite associated with titanite.

262 (iii) Metagreywacke: it is the dominant lithology at Kiaka and forms the southern  
263 footwall of a D2-related shear zone hosting the main mineralized zone. Composed of quartz,  
264 feldspar, and sillimanite with a granoblastic texture, metagreywacke locally contain  
265 disseminated tourmaline grains (*Tur<sub>2</sub>*), about 50 µm in size (Fig. 3C-D). Sample KDH29 (depth  
266 311.8 m; Fig. 3C-D; Fig. 4) is from a phlogopite-rich alteration zone close to the orebody.

267 (iv) Metamafic rock: it is intercalated within the metasedimentary sequence forming  
268 >50 m thick sequences dipping towards the northwest (Fig. 1). Sample KDH291 (depth 56.2

269 m; Fig. 3E-F) comes from an alteration zone in proximity to the mineralized envelope. Within  
270 this zone, the metamafic rock contains porphyroblasts of hydrothermal tourmaline (*Tur*<sub>2</sub>)  
271 reaching few millimeters in size, embedded within a chloritized, fine-grained matrix, that  
272 locally contains pyrrhotite, titanite and clinozoisite (Fig. 3E).

273

#### 274 **Scanning electron microscopy**

275 Mineralogical observations of tourmaline were carried out using transmitted-light microscopy  
276 and scanning electron microscopy (SEM) at the GeoRessources laboratory (Nancy, France).  
277 Tourmaline grains were investigated using a Hitachi S-4800 and a JEOL J7600F scanning  
278 electron microscopes, both equipped with SDD-type energy-dispersive X-ray spectrometers  
279 (EDS). Backscattered electron (BSE) images were acquired on carbon-coated polished thin  
280 sections with an acceleration voltage of 15 kV, adjusting the image contrast to reveal internal  
281 zoning within the tourmaline grains. SEM was used to characterize the internal textures of  
282 tourmaline and to select representative grains for the *in situ* chemical and isotopic analyses.

283

#### 284 **Electron probe microanalysis**

285 Major and minor element composition of tourmaline was determined using a Cameca SX100  
286 electron microprobe analyzer (EMPA) equipped with five wavelength-dispersive X-ray  
287 spectrometers (WDS) at the GeoRessources laboratory (Nancy, France). Analyses were  
288 performed with the following operating conditions: beam current of 20 nA, acceleration voltage  
289 of 15 kV, and beam diameter of 1 μm. Counting times on element peaks and backgrounds were  
290 16 sec and 8 sec, respectively, for Si, Al, K, Ca, Fe, Mg, Mn, Ti, and 30 sec and 15 sec,  
291 respectively, for Na, Cr, and Cl. The following standards and monochromators were used for  
292 the EMPA measurements: albite (Si, Na on TAP), olivine (Mg on TAP), corundum (Al on  
293 TAP), orthoclase (K on LPET), andradite (Ca on PET), ilmenite (Ti on LPET, Mn on LIF),

294 hematite (Fe on LIF), and vanadinite (Cl on LPET). Detection limits are approximately 330  
295 ppm for Si, 300 ppm for Al, 1000 ppm for Fe, 265 ppm for Mg, 250 ppm for Ti, 365 ppm for  
296 Mn, 515 ppm for Na, 370 ppm for Ca, 200 ppm for K, and 140 ppm for Cl. Structural formulae  
297 of tourmaline were calculated using the WinTcac software (Yavuz et al. 2014) normalizing to  
298 15 cations in Y+Z+T sites and assuming stoichiometric 3 atoms for B and 4 atoms for OH+F,  
299 based on the general formula  $XY_3Z_6(T_6O_{18})(BO_3)_3V_3W$ , where X = Na<sup>+</sup>, Ca<sup>2+</sup>, K<sup>+</sup>, or vacancy  
300 site; Y = Fe<sup>2+</sup>, Mg<sup>2+</sup>, Mn<sup>2+</sup>, Al<sup>3+</sup>, Li<sup>+</sup>, Fe<sup>3+</sup>, or Cr<sup>3+</sup>; Z = Al<sup>3+</sup>, Fe<sup>3+</sup>, Ti<sup>4+</sup>, Mg<sup>2+</sup>, or Cr<sup>3+</sup>; T = Si<sup>4+</sup>,  
301 Al<sup>3+</sup>, or B<sup>3+</sup>; V = OH<sup>-</sup>, O<sup>2-</sup>; and W = OH<sup>-</sup>, F<sup>-</sup>, or O<sup>2-</sup> (Henry et al. 2011). Chemical compositions  
302 of tourmaline are reported in weight per cent (wt.%) oxides and the structural formulae are  
303 expressed in atoms per formula unit (apfu) (ESM Table 2). X-ray elemental maps were acquired  
304 with a 15 kV accelerating voltage, a 100 nA beam current, and a 1  $\mu\text{m}^2$  electron beam (Fig. 6).  
305 The elements Na, Si, Mg, Al, Ca, Ti, and Fe were measured with dwell times of 300 msec each  
306 and an acquisition step of 10  $\mu\text{m}$ , for a total map size of 2900 x 3890  $\mu\text{m}$ .

307

### 308 **Secondary ion mass spectrometry**

309 Boron isotopic composition of tourmaline was measured by secondary ion mass spectrometry  
310 (SIMS) using a Cameca IMS 1280-HR instrument at the CRPG-CNRS (Vandoeuvre-lès-  
311 Nancy, France). Analyses were performed on gold-coated polished thin sections that were  
312 previously investigated by SEM and EMPA, with a 20 nA beam of primary ions O<sup>-</sup> accelerated  
313 at 13 kV with an ellipsoid ablation spot of 20  $\mu\text{m}$  long axis. The secondary ions <sup>10</sup>B<sup>+</sup> and <sup>11</sup>B<sup>+</sup>  
314 were accelerated at 10 kV and were measured in mono-collection with the axial Faraday cup  
315 with a mass resolution power  $M/\Delta M = 2000$ . Each calculated isotopic ratio <sup>11</sup>B/<sup>10</sup>B corresponds  
316 to 30 cycles of measurement with counting times of 8 sec per cycle on mass 10 and of 4 sec per  
317 cycle on mass 11. For each spot, a pre-sputtering of 60 sec was applied immediately before  
318 each analysis for surface cleaning. Instrumental mass fractionation (IMF) was determined and

319 corrected using two tourmaline reference materials corresponding to dravite (Harvard #108796)  
320 and schorl (Harvard #112566) described by Dyar et al. (2001) and Leeman and Tonarini (2001).  
321 Each standard was measured several times during the analytical SIMS session following a  
322 standard-sample bracketing procedure. The summary of the B isotope analyses on the  
323 tourmaline reference materials measured by SIMS is reported in ESM Table 1. The matrix  
324 effect was corrected using the dravite Harvard #108796 reference material because the  
325 tourmaline samples analyzed in this work have dravitic composition. After correction of IMF,  
326 the measured  $^{11}\text{B}/^{10}\text{B}$  ratios were reported in  $\delta^{11}\text{B}$  notation (in ‰) relative to the NIST SRM  
327 951, whose  $^{11}\text{B}/^{10}\text{B}$  ratio is 4.04362 (Catanzaro et al. 1970). The external error ( $2\sigma$ ) is about  
328 0.13‰ over 28 analyses for the dravite Harvard #108796 and 0.26‰ over 14 analyses for the  
329 schorl Harvard #112566. The external error used is that of the dravite Harvard #108796. The  
330 total error is the quadratic sum of the internal and external errors and range between 0.2 and  
331 1.2‰ ( $2\sigma$ ) on the tourmaline samples with a median value of 0.3‰ ( $2\sigma$ ).

332

### 333 **Multi-collector – inductively coupled plasma – mass spectrometry**

334 Whole-rock boron content and isotopic compositions of the muscovite schist and diorite were  
335 measured using a Thermo Scientific Neptune multi-collector – inductively coupled plasma –  
336 mass spectrometer (MC-ICP-MS) at the LhyGeS (Université de Strasbourg-EOST, France).  
337 The B extraction procedure was adapted from Lemarchand et al. (2012) and is summarized as  
338 follows: 10 mg of powdered sample were mixed with 250 mg of analytical grade  $\text{K}_2\text{CO}_3$  in a  
339 12 mL PtAu 05 crucible and placed in a muffle furnace at  $950^\circ\text{C}$  for 45 min. After cooling, the  
340 fusion residue was dissolved in 35 mL of bidistilled HCl 0.2N. Boron was then purified from a  
341 0.5 mL aliquot by a two-step chemical procedure using the cation exchange resin Biorade  
342 AG50WX12 and the B-specific resin Amberlite IRA743. The recovered solution was  
343 simultaneously analyzed for both B concentration and isotope ratios using the standard-sample-

344 standard bracketing method. The operational settings for B analyses by MC-ICP-MS are  
345 described in details by Roux et al. (2015). Accuracy has been verified by repeated analyses of  
346 solution and rock standards (ERM AE120 = -20.1‰; ERM AE121 = +20.0‰; NRC NASS5  
347 = +39.8‰; GSJ JB2 = +7.2‰). Total B contamination is 15 ng and the analytical uncertainties  
348 are 5% and 0.4‰ (2σ) for B concentration and isotope ratios, respectively.

349

## 350 **RESULTS**

351

### 352 **Petrography and textural features of tourmaline**

353 Hydrothermal tourmaline ( $Tur_2$ ) hosted in metagreywacke (sample KDH29-311.8 m; 1.08 g/t  
354 Au) ranges in size from 20 to 400 μm with euhedral to sub-euhedral shapes (Fig. 3C-D; Fig. 4).  
355 No foliation is clearly preserved in this sample. A metamorphic recrystallization can be  
356 observed whereas  $Tur_2$  and biotite seem to represent a mineral equilibrium assemblage and to  
357 be part of the same hydrothermal D2<sub>Ki</sub> event. In addition, pyrrhotite and pyrite are characteristic  
358 of the assemblage of the low-grade disseminated ore in the Kiaka deposit. The tourmaline grains  
359 in the metagreywacke sample occasionally host micro-inclusions of apatite, quartz and  
360 pyrrhotite oriented along intra-grain fractures. At microscopic scale, tourmaline has light green  
361 to brownish colors in polarized light and is greenish in crossed polarized light. The grains  
362 appear homogeneous without core-rim zoning on BSE images (Fig. 4). Nine representative  
363 tourmaline grains were selected for *in situ* chemical and isotopic analyses.

364 Hydrothermal tourmaline ( $Tur_2$ ) hosted in metamafic rock (sample KDH291-56.2 m; 0.05 g/t  
365 Au) is characterized by euhedral to sub-euhedral habit and is commonly millimetric in size (Fig.  
366 3E). Under the microscope, poikiloblastic tourmaline porphyroblasts have light yellow to beige  
367 colors in polarized light and are yellow-brownish in crossed polarized light. Three  
368 representative millimetre-size tourmaline grains intergrown with the biotite-titanite-clinozoisite



369 D2<sub>Ki</sub> assemblage were selected for the *in situ* chemical and isotopic analyses (Fig. 5). Those  
370 three grains show different crystal orientation relative to the thin section plane, and their internal  
371 zoning and compositional variations were investigated in detail. The first tourmaline grain  
372 (Grain 1) shows an oblique section relative to the c-axis of about 3 mm wide, the second (Grain  
373 2) shows a transversal section relative to the c-axis of about 9 mm in length, and the third (Grain  
374 3) shows an oblique section relative to the c-axis (Fig. 5). The poikiloblastic tourmaline  
375 porphyroblasts host numerous sulfide inclusions (<100 μm up to 0.1 mm in size), including  
376 pyrrhotite, chalcopyrite and pyrite, as well as accessory clinozoisite, biotite, amphibole, and  
377 chlorite (Chl 2) (Fig. 2). At the grain scale, tourmaline hosted in metamafic rock shows a core-  
378 rim zoning on BSE images (Fig. 5C). The core represents the main part of the grains and shows  
379 a patchy zoning with dark to medium grey contrasts on BSE images. The rim forms a 100-300  
380 μm thick overgrowth in optical continuity with the core and shows brighter contrasts on BSE  
381 images. No dissolution textural evidence between core and rim was observed. X-ray elemental  
382 maps show intra-crystalline chemical zoning for Al, Fe, Mg, Ca, and Ti (Fig. 6). The rim is  
383 marked by higher Fe contents relative to the core, which is Mg-rich. The intra-grain variation  
384 in Ca, Ti, and Al, corresponds to the patchy zoning within the core related to the primary crystal  
385 growth of tourmaline.

386

### 387 **Chemical composition of tourmaline**

388 Chemical compositions and structural formulae of representative tourmaline grains (*Tur2*) from  
389 the Kiaka deposit are reported in the ESM Table 2. Overall, tourmaline compositions show  
390 relatively large variations in major elements for FeO (4.65-7.68 wt.%), MgO (7.10-9.52 wt.%),  
391 Al<sub>2</sub>O<sub>3</sub> (29.59-35.20 wt.%), and relatively small variations in minor elements for Na<sub>2</sub>O (1.41-  
392 1.70 wt.%), CaO (0.58-2.10 wt.%), MnO (<0.1 wt.%), and TiO<sub>2</sub> (0.19-1.51 wt.%). The

393 measured K<sub>2</sub>O and Cl values are very low (up to 0.14 wt.%), close to or below the EMPA limits  
394 of detection.

395 Tourmaline hosted in the metamafic rock (sample KDH291-56.2 m) belongs to the alkali-group  
396 and plots within the compositional field of Al-poor and Fe<sup>3+</sup>-rich metasedimentary rocks in the  
397 Al-Fe-Mg diagram (Fig. 7F). Tourmaline has a dravite composition with Mg/(Fe+Mg) = 0.67-  
398 0.77 and X<sub>vacancy</sub>/(X<sub>vacancy</sub>+Na) = 0.11-0.29 (Fig. 7A). It has moderate contents of Ca (0.10-0.64  
399 apfu), Na (0.50-0.70 apfu), and Al (5.55-6.27 apfu). No correlation is found between the Ca  
400 and Ti contents (0.04-0.19 apfu) and the color zoning of tourmaline in polarized light. The core  
401 and rim show minor compositional variations that are principally marked by variations of the  
402 Fe/Mg ratio, as also seen on X-ray elemental maps (Fig. 6). The chemical variations for  
403 tourmaline hosted in the metamafic rock are mostly due to the Mg<sub>+1</sub>Fe<sub>-1</sub> and □Al<sub>+1</sub>(NaMg)<sub>-1</sub>  
404 exchange vectors, with possible contribution of the (AlO)<sub>+1</sub>(MgOH)<sub>-1</sub> deprotonation vector  
405 (Fig. 7).

406 Tourmaline hosted in the metagreywacke (sample KDH29-311.8 m) has a distinct chemical  
407 composition compared to the metamafic rock-hosted tourmaline. Tourmaline belongs to the  
408 alkali-group with a dravite composition and plots into the compositional field of Al-rich  
409 metasedimentary rocks in the Al-Fe-Mg diagram (Fig. 7F). It differs mainly from tourmaline  
410 hosted in the metamafic rock by lower contents of Ca (0.16-0.22 apfu), Mg (1.75-1.89 apfu),  
411 and Na (0.45-0.54 apfu), and by higher contents of X-vacancy (0.25-0.35 apfu), and Al (6.37-  
412 6.72 apfu). Tourmaline has dravite composition with Mg/(Fe+Mg) = 0.68-0.73 and  
413 X<sub>vacancy</sub>/(X<sub>vacancy</sub>+Na) = 0.32-0.44. Variations of tourmaline compositions are mostly explained  
414 by the Mg<sub>+1</sub>Fe<sub>-1</sub> and □Al<sub>+1</sub>(NaMg)<sub>-1</sub> exchange vectors joining the dravite to foitite endmembers  
415 (Fig. 7B-C).

416

417 **Boron isotope composition of the host rocks and tourmaline**

418 Whole-rock boron isotope analyses were carried out on representative samples of unaltered  
419 diorite (sample KDH337-44.1) and muscovite schist (sample KDH75-64.9) collected outside  
420 the mineralized envelopes. Boron concentration and isotope analyses yielded reproducible  
421 values for each sample (Table 1). The diorite has a B content of 5.6 ppm with an average  $\delta^{11}\text{B}$   
422 value of  $-13.9\text{‰}$  ( $n = 2$ ), whereas the muscovite schist contains 71 ppm B and has an average  
423  $\delta^{11}\text{B}$  value of  $-29.2\text{‰}$  ( $n = 2$ ). Because the samples are devoid of hydrothermal alteration and  
424 the isotopic data are reproducible, the whole-rock boron isotope compositions are considered  
425 to be representative of each rock precursor.

426 *In situ* boron isotope compositions of tourmaline hosted in the metagreywacke (sample KDH29-  
427 311.8 m) and the metamafic rock (sample KDH291-56.2 m) are shown in Fig. 8 and Table 2.  
428 The full range of  $\delta^{11}\text{B}$  values of tourmaline extends from  $-25.12\text{‰}$  to  $-15.10\text{‰}$  ( $n = 49$ ) and  
429 overlaps the lower  $\delta^{11}\text{B}$  range of tourmaline hosted in orogenic gold deposits worldwide ( $\delta^{11}\text{B}$   
430 =  $-24\text{‰}$  to  $+19\text{‰}$ ; Fig. 8). Tourmaline hosted in the metamafic rock has heavier boron isotopic  
431 composition ( $\delta^{11}\text{B} = -19.6\text{‰}$  to  $-15.1\text{‰}$ ; mean =  $-17.8\text{‰}$ ; mode  $\sim -19.5\text{‰}$ ;  $n = 31$ ) compared  
432 to tourmaline hosted in the metagreywacke ( $\delta^{11}\text{B} = -25.1\text{‰}$  to  $-22.0\text{‰}$ ; mean =  $-24.2\text{‰}$ ; mode  
433  $\sim -24.0\text{‰}$ ;  $n = 18$ ). Isotopic analyses of single tourmaline grains reveal  $\delta^{11}\text{B}$  variations up to  
434  $4.7\text{‰}$  from core to rim, but show no systematic  $\delta^{11}\text{B}$  variation related to sector and patchy  
435 zoning. No correlation was found between the chemical and boron isotopic composition of  
436 tourmaline.

437

## 438 **DISCUSSION**

439

### 440 **Chemical composition of tourmaline as a monitor of fluid-rock interactions**

441 Tourmaline grains hosted in the metamafic rock and the metagreywacke belong to the dravite  
442 series, but they differ by their chemical and boron isotopic compositions. Tourmaline hosted in

443 the metamafic rock is Al-poor (5.75-6.27 apfu), Fe-rich (0.63-1.05 apfu) and Mg-rich (2.00-  
444 2.30 apfu), whereas tourmaline hosted in metagreywacke is Al-rich (6.37-6.72 apfu), Fe-poor  
445 (0.65-0.83 apfu) and Mg-poor (1.75-1.89 apfu). This is consistent with the whole-rock contents  
446 of Al<sub>2</sub>O<sub>3</sub>, Fe<sub>2</sub>O<sub>3</sub> and MgO in metamafic rock and metagreywacke, respectively (Table 1;  
447 Fontaine et al. 2017), which suggests a host rock control on the chemical composition of  
448 tourmaline (except for boron), as proposed by other studies (e.g. van Hinsberg et al. 2011;  
449 Hazarika et al. 2015; 2016; Kalliomäki et al. 2017; Harlaux et al. 2019). In addition, metamafic  
450 rock-hosted tourmaline has lower X-vacancy contents (0.08-0.24 apfu) and higher Na+Ca  
451 contents (0.76-0.92 apfu), whereas metagreywacke-hosted tourmaline has higher X-vacancy  
452 contents (0.25-0.35 apfu) and lower Na+Ca contents (0.65-0.75 apfu). This is also consistent  
453 with the higher whole-rock contents of CaO, Na<sub>2</sub>O and K<sub>2</sub>O in the metamafic rock compared  
454 to metagreywacke (Table 1; Fontaine et al. 2017). In the X-vacancy vs. Al total and Fe vs. Al  
455 diagrams (Fig. 7C, D), metamafic rock-hosted tourmaline shows large Al variations (5.75-6.27  
456 apfu) reflecting the (AlO)<sub>+1</sub>(MgOH)<sub>-1</sub> deprotonation exchange vector, whereas metagreywacke  
457 tourmaline has higher Al and X-vacancy contents projecting along the □Al<sub>+1</sub>(NaMg)<sub>-1</sub> exchange  
458 vector.

459 These variations may reflect variable degrees of interaction between the hydrothermal fluid and  
460 the host rocks. For comparison, syn-ore hydrothermal tourmaline from orogenic gold deposits  
461 in the Loulo Gold District in Mali (Lambert-Smith et al. 2016) shows large variations of the  
462 Mg/(Fe+Mg) ratio (0.27-0.96) and have lower Ca contents (0.01-0.09 apfu) and higher Na  
463 contents (0.62-0.89) compared to hydrothermal tourmaline from Kiaka (Fig. 7). The  
464 composition of the X-site in tourmaline is dominantly controlled by the Na and Ca  
465 concentrations in the coexisting aqueous fluid, being therefore a function of the fluid salinity  
466 (von Goerne et al. 2001, 2011; Dutrow and Henry 2016, 2018). The relative high contents of  
467 Na (0.45-0.70 apfu, average = 0.61 apfu) and Ca (0.10-0.37 apfu, average = 0.24 apfu) and the

468 relative low contents of X-vacancy (0.08-0.35 apfu, average = 0.15 apfu) in hydrothermal  
469 tourmaline (*Tur*<sub>2</sub>) suggest that the fluid was of low to moderate salinity. The tourmaline-bearing  
470 ore assemblage is interpreted to have formed during the D2<sub>Ki</sub> stage at temperatures of 371-  
471 413°C based on chlorite (Chl 2) thermometry (Fontaine et al. 2017). Additionally, arsenopyrite  
472 in contact with pyrrhotite and löllingite in quartz-biotite metagreywacke contains 35.4-36.5  
473 atm% of As, yielding temperatures of 360-475°C (Fontaine et al. 2017). Assuming a median  
474 temperature of 400°C and an average Na = 0.6 apfu in tourmaline, a salinity of ca. 3 wt.% NaCl  
475 equiv can be estimated for the fluid in equilibrium with the assemblage tourmaline + quartz +  
476 chlorite (von Goerne et al. 2001). Tourmaline precipitation from hydrothermal fluids requires  
477 acidic to near-neutral conditions (pH <6) that favor the formation of stable trigonal complexes  
478 [B(OH)<sub>3</sub>] in the fluid (Morgan and London 1989; Henry and Dutrow 1996). The development  
479 of pervasive sericitization associated with disseminated tourmaline and clinozoisite in the  
480 metagreywacke (Fontaine et al. 2017) suggests that the fluid was moderately acidic. The  
481 composition of tourmaline from Kiaka is dominantly controlled by the Fe<sup>2+</sup><sub>+1</sub>Mg<sup>2+</sup><sub>-1</sub> and  
482 □Al<sub>+1</sub>(NaMg)<sub>-1</sub> exchange vectors with no contribution of the Fe<sup>3+</sup><sub>+1</sub>Al<sup>3+</sup><sub>-1</sub> homovalent  
483 substitution (Fig. 7), which suggests low Fe<sup>3+</sup>/Fe<sup>2+</sup> ratios and reduced fluid conditions. These  
484 arguments suggest that hydrothermal tourmaline (*Tur*<sub>2</sub>) likely formed from moderately high  
485 temperature (ca. 400°C), moderately acidic, reduced, and low-salinity hydrothermal fluids and  
486 that its chemical composition (except for B, Na and Ca) was buffered by the host rock during  
487 fluid-rock interactions.

488

#### 489 **Origin of fluids and boron for formation of the Kiaka gold deposit**

490 The source of boron and mineralizing fluids at Kiaka can be discussed in terms of proximal vs.  
491 distal, as well as magmatic vs metamorphic origin. In the metagreywacke and the metamafic  
492 rock, the boron budget is largely dominated by hydrothermal tourmaline (*Tur*<sub>2</sub>), which is the

493 main boron-bearing mineral in those rocks. Considering that basalts have typically very low  
494 boron contents (Table 1; <0.1 to 5 ppm; Leeman and Sisson 1996; Marschall 2018), it is  
495 unlikely that the boron required to form *Tur*<sub>2</sub> in the metamafic rock was derived from the  
496 basaltic precursor. The metagreywacke contains two generations of tourmaline: one generation  
497 is detrital (*Tur*<sub>1</sub>), being part of the mineral assemblage of the protolith, whereas the other one is  
498 hydrothermal (*Tur*<sub>2</sub>), being formed during the D2<sub>KI</sub> event. As detrital *Tur*<sub>1</sub> remained stable in  
499 the metagreywacke during the prograde and retrograde metamorphism, it seems unlikely that  
500 *Tur*<sub>1</sub> was a viable source of boron for formation of *Tur*<sub>2</sub>, even if we cannot definitively exclude  
501 the potential destabilization of *Tur*<sub>1</sub> in deep-seated metagreywacke lithologies.

502 We may also exclude the diorite as a proximal boron source because of its low boron content  
503 (B = 5.6 ppm, Table 1) and its absence of significant hydrothermal alteration, arguing against  
504 the release of boron-rich magmatic fluids or post-magmatic hydrothermal alteration. Another  
505 possible candidate could be the younger unfoliated biotite granites that have intruded the TTG  
506 basement between ca. 2120 Ma and 2100 Ma (Vegas et al. 2008; Baratoux et al. 2011). These  
507 granitic rocks emplaced through transcurrent shearing along the Manga Fada N’Gourma  
508 greenstone belt and the related amphibolite-facies metamorphism attributed to contact  
509 metamorphism (Naba et al. 2004; Vegas et al. 2008) has been dated at 2105 ± 30 Ma (Pb-Pb on  
510 zircon; Castaing et al. 2003). However, none of these granitic rocks has been described in the  
511 district of Kiaka and no granite intercept was found in the investigated drill cores.

512 A proximal origin of boron-rich fluids may therefore be discarded. The boron isotope  
513 compositions of hydrothermal tourmaline (*Tur*<sub>2</sub>) from Kiaka ( $\delta^{11}\text{B} = -25.1\text{‰}$  to  $-15.1\text{‰}$ ; Fig.  
514 8) fall outside the typical  $\delta^{11}\text{B}$  range for tourmaline hosted in granitic rocks ( $-15\text{‰}$  to  $+5\text{‰}$ ;  
515 Marschall and Jiang 2011; Trumbull and Slack 2018), although they partly overlap with the  
516  $\delta^{11}\text{B}$  range of tourmaline from granite-related veins ( $-22\text{‰}$  to  $-3\text{‰}$ ; Fig. 8).

517 A magmatic-hydrothermal origin of the fluid can be excluded, because (i) no contemporaneous  
518 granitic intrusion is found nearby the Kiaka deposit, (ii) age constraints exclude the diorite plug  
519 as a magmatic source of boron, and, to a lesser extent, (iii) the mineralization is hosted in thick  
520 metasedimentary-metavolcanic units. A meta-evaporitic fluid origin ( $\delta^{11}\text{B} = +5\text{‰}$  to  $> +30\text{‰}$ )  
521 can also be ruled out. In contrast, the B isotope values of *Tur*<sub>2</sub> are compatible with those of  
522 tourmaline hosted in metasedimentary rocks ( $\delta^{11}\text{B} = -26\text{‰}$  to  $+1\text{‰}$ ; Nakano and Nakamura  
523 2001; Bebout and Nakamura 2003; Marschall and Jiang 2011; Berryman et al. 2017; Fig. 8).  
524 Despite the general diachronism observed from east to west in the southern WAC (Parra-Avila  
525 et al. 2017), comparison with the Loulo Mining District in Mali is of interest. Lambert-Smith  
526 et al. (2016) have used geochemistry and boron isotopy of tourmaline to discriminate fluid  
527 source regions. The  $\delta^{11}\text{B}$  values in syn-ore tourmaline indicate a dominant fluid contribution  
528 from clastic metasediments and carbonate rocks, suggesting metamorphic devolatilization in  
529 the host terrane as the most likely process that produced the ore-forming fluids. It seems likely  
530 for the Kiaka deposit that hydrothermal tourmaline crystallized from a boron-rich metamorphic  
531 fluid, of distal origin, derived from deep-seated metasediments.

532 Boron isotope compositions of tourmaline hosted in the metamafic rock ( $\delta^{11}\text{B} = -19.6\text{‰}$  to -  
533  $15.1\text{‰}$ ) and the metagreywacke ( $\delta^{11}\text{B} = -25.1\text{‰}$  to  $-22.0\text{‰}$ ) show a significant difference of  
534  $\delta^{11}\text{B}$  values (up to  $10\text{‰}$ ), which suggests variable degrees of interactions between the boron-  
535 rich hydrothermal fluid and the host rocks, as also supported by the chemical compositions of  
536 tourmaline. The muscovite schists may represent a potential source for the boron-rich fluids  
537 because they have a relatively high B content (71 ppm, Table 1), which is commonly associated  
538 with micas (Leeman and Sisson 1996; Nakano and Nakamura 2001; Trumbull and Slack 2018).  
539 Muscovite breakdown reactions in metapelitic rocks at  $P \leq 4$  kbar and  $T \leq 650^\circ\text{C}$  (Thompson  
540 1982; Vielzeuf and Holloway 1988; Spear et al. 1999) can produce a low-salinity, reduced, and  
541 boron-rich metamorphic fluid (Moran et al. 1992; Henry and Dutrow 1996; Nakano and

542 Nakamura 2001; Kawakami and Ikeda 2003). In order to evaluate whether hydrothermal  
543 tourmaline could have formed from boron-rich fluids derived from devolatilization of  
544 muscovite schists at depth, we calculated the tourmaline-fluid B isotope fractionation according  
545 to the Rayleigh fractionation model of Marschall et al. (2009) and using the fractionation factors  
546 of Meyer et al. (2008). Considering a temperature of 650°C for the muscovite breakdown  
547 reaction, an average  $\delta^{11}\text{B} = -29.2\text{‰}$  for the muscovite schist (Table 1), and a muscovite-fluid  
548 boron isotopic fractionation of  $-7.7\text{‰}$  (Wunder et al. 2005), we estimated a  $\delta^{11}\text{B} = -21.5\text{‰}$  for  
549 the expelled metamorphic fluid. At 650°C, the minimum boron content of this fluid would be  
550 about 1.0 to 2.5 wt.%  $\text{B}_2\text{O}_3$  (London 2011). The evolution of the B isotopic composition of this  
551 fluid during its ascent through metamorphic rocks at amphibolite facies conditions was  
552 calculated using the fractionation for a stepwise decreasing temperature from 650 to 350°C  
553 following the model of Büttner et al. (2016). Considering an initial fluid composition of  $\delta^{11}\text{B} =$   
554  $-21.5\text{‰}$  at 650°C, progressive fractionation by removing 60 to 90% of boron from the fluid ( $F$   
555  $= 0.1\text{--}0.4$ ) results in a shift towards higher  $\delta^{11}\text{B}$  values of  $-19.6\text{‰}$  to  $-14.9\text{‰}$  (Fig. 9).  
556 Tourmaline precipitating from this fluid would acquire  $\delta^{11}\text{B}$  compositions comprised between  
557  $-20\text{‰}$  and  $-18\text{‰}$ . At 400°C, a representative temperature for  $Tur_2$  formation at Kiaka, the fluid  
558 would have a  $\delta^{11}\text{B} = -16.3\text{‰}$  and the corresponding tourmaline would acquire a  $\delta^{11}\text{B} = -19.1\text{‰}$   
559 (Fig. 7). These  $\delta^{11}\text{B}$  values fall into the range of  $\delta^{11}\text{B} = -25.1\text{‰}$  to  $-15.1\text{‰}$  (average =  $-20.1\text{‰}$ )  
560 measured for hydrothermal tourmaline from Kiaka. The differences of  $\delta^{11}\text{B}$  values between  
561 tourmaline hosted in the metagreywacke (average =  $-24.2\text{‰}$ ) and the metamafic rock (average  
562 =  $-17.8\text{‰}$ ) are interpreted to reflect variable degrees of interactions, at constant temperature  
563 (ca. 400°C), between the host rocks of initially distinct isotopic compositions and the boron-  
564 rich metamorphic fluid.

565 In summary, hydrothermal tourmaline ( $Tur_2$ ) from Kiaka formed through moderately high-  
566 temperature fluid-rock interactions between boron-rich metamorphic fluids and the country



567 rocks, resulting in the local uptake of Al, Fe, and Mg required for tourmaline formation. We  
568 propose that the source of the boron-rich fluids was derived from muscovite schists similar to  
569 those exposed at Kiaka but located at a deeper level in the metamorphic nappe. The present  
570 results indicate that neither proximal country rocks of the Kiaka deposit nor ascending granitic  
571 magmas could be viable sources of fluids and boron. However, the isotopic data are consistent  
572 with fluids and boron being issued from devolatilization of deep-seated muscovite schists  
573 during the D2<sub>Ki</sub> event, which relates to the prograde-to-peak amphibolite facies regional  
574 metamorphism. This interpretation is supported by mineral-equilibria modelling suggesting that  
575 exhumation of metasediments can produce important amounts of metamorphic fluids at  
576 temperatures near 500°C (Vry et al. 2010).

577

## 578 **CONCLUSIONS**

579 In the Kiaka orogenic gold deposit, hydrothermal tourmaline (*Tur*<sub>2</sub>) is commonly associated  
580 with the proximal alteration assemblage in the host rocks. Mineralogical observations suggest  
581 that deposition of *Tur*<sub>2</sub> was synchronous with the early sulfide-rich disseminated gold  
582 mineralization coeval with the D2<sub>Ki</sub> phase, corresponding to the regional prograde-to-peak  
583 metamorphism. Hydrothermal tourmaline hosted in metamafic rock and metagreywacke has a  
584 dravite composition, but shows variable major element contents, mainly in Al, Mg, and Fe, thus  
585 suggesting a host rock buffering. Boron isotope compositions of tourmaline range between -  
586 25.1‰ and -15.1‰, with differences between tourmaline hosted in the metamafic rock ( $\delta^{11}\text{B} =$   
587  $-19.6\text{‰}$  to  $-15.1\text{‰}$ ) and tourmaline hosted in the metagreywacke ( $\delta^{11}\text{B} = -25.1\text{‰}$  to  $-22.0\text{‰}$ ).  
588 Modeling of tourmaline-fluid boron isotope fractionation argue for a metamorphic origin of the  
589 mineralizing fluids that were produced during devolatilization of deep-seated muscovite schists.  
590 We propose that hydrothermal tourmaline (*Tur*<sub>2</sub>) and the synchronous disseminated gold  
591 mineralization resulted from moderately high-temperature (ca. 400°C) interactions between a

592 boron-rich hydrothermal fluid and the metamorphic host rocks at recorded amphibolite facies  
593 conditions.

594

#### 595 **Acknowledgments**

596 We are grateful to AMIRA International and industry sponsors, including AusAid and the ARC  
597 Linkage Project LP110100667, for their support on the WAXI project (P934A). This study is  
598 part of the WAXI 2 program (<http://waxi2.org/>). We also thank Drs. James Lambert-Smith and  
599 Crystal LaFlamme for their constructive and thorough reviews that greatly helped improving  
600 the quality of the original manuscript. Finally, we thank the Editor-in-Chief Dr. Georges  
601 Beaudoin and the Guest Editor Dr. Nicolas Thébaud for their comments and the editorial  
602 handling.

603 **References**

- 604 Abouchami W, Boher M, Michard A, Albarede F (1990) A major 2.1 Ga event of mafic  
605 magmatism in west Africa: An Early stage of crustal accretion. *J Geophys Res Solid Earth*  
606 95:17605-17629
- 607 Allibone A, Hayden P, Cameron G, Duku F (2004) Paleoproterozoic Gold Deposits Hosted by  
608 Albite- and Carbonate-Altered Tonalite in the Chirano District, Ghana, West Africa. *Econ*  
609 *Geol* 99:479-497
- 610 Anglin CD, Jonasson IR, Franklin JM (1996) Sm-Nd dating of scheelite and tourmaline;  
611 implications for the genesis of Archean gold deposits, Val d'Or, Canada. *Econ Geol*  
612 91:1372-1382
- 613 Augustin J, Gaboury D, (2017) Paleoproterozoic plume-related basaltic rocks in the Mana gold  
614 district in western Burkina Faso, West Africa: Implications for exploration and the source  
615 of gold in orogenic deposits. *J Afr Sci* 129:17-30
- 616 Augustin J, Gaboury D, Crevier M (2017) Structural and gold mineralizing evolution of the  
617 world-class orogenic Mana district, Burkina Faso: Multiple mineralizing events over 150  
618 million years. *Ore Geo Rev* 91:981-1012
- 619 Baksheev, IA, Prokofiev VY, Trumbull RB, Wiedenbeck M, Yapaskurt VO (2015)  
620 Geochemical evolution of tourmaline in the Darasun gold district, Transbaikal region,  
621 Russia: evidence from chemical and boron isotopic compositions. *Miner Deposita*  
622 50:125-138
- 623 Baratoux L, Metelka V, Naba S, Jessel MW, Gregoire M, Ganne J (2011) Juvenile  
624 Paleoproterozoic crust evolution during the Eburnean orogeny (2.2-2.0 Ga), western  
625 Burkina Faso. *Precambrian Res* 191:18-45

- 626 Beaudoin G, Rollion-Bard C, Giuliani G (2013) The boron isotope composition of tourmaline  
627 from the Val-d'Or orogenic gold deposits, Québec, Canada. 12<sup>th</sup> SGA Biennial Meeting:  
628 Mineral deposit research for a high-tech world 3:1090-1092
- 629 Bebout GE, Nakamura E (2003) Record in metamorphic tourmalines of subduction-zone  
630 devolatilization and boron cycling. *Geology* 31:407-410
- 631 Berryman EJ, Kutzschbach M, Trumbull RB, Meixner A, van Hinsberg V, Kasemann SA,  
632 Franz G (2017) Tourmaline as a petrogenetic indicator in the Pfitsch Formation, Western  
633 Tauern Window, Eastern Alps. *Lithos* 284:138-155
- 634 Béziat D, Bourges F, Debat P, Fuchs Y, Lompo M, Martin F, Kiema S, Tollon F (1999) The  
635 Guibaré and Fété Kolé gold-bearing tourmaline-quartz veins in the Birimian greenstone  
636 belt of Burkina Faso. *Can Mineral* 37:575-591
- 637 Béziat D, Dubois M, Debat P, Nikiéma S, Salvi S, Tollon F (2008) Gold metallogeny in the  
638 birimian craton of Burkina Faso (West Africa). *J Afr Earth Sci* 50:215-233
- 639 Block S, Ganne J, Baratoux L, Zeh A, Parra-Avila A, Jessel M, Ailleres L, Siebenaller L (2015)  
640 Petrological and geochronological constraints on lower crust exhumation during  
641 Paleoproterozoic (Eburnean) orogeny, NW Ghana, West African Craton, *Journal of*  
642 *Metamorphic Geology* 33:463-494
- 643 Block S, Baratoux L, Zeh A, Laurent O, Bruguier P, Jessel M, Ailleres L, Sagna R, Parra-Avila  
644 LA, Bosch D (2016) Paleoproterozoic juvenile crust formation and stabilisation in the  
645 south-eastern West African Craton (Ghana); New insights from U-Pb-Hf zircon data and  
646 geochemistry. *Precambrian Res* 287:1-30
- 647 Boher M, Abouchami W, Michard A, Albarede F, Arndt NT (1992) Crustal growth in West  
648 Africa at 2.1 Ga. *J Geophys Res Solid Earth* 97:345-369

649 Burrows D, Spooner E (1987) Generation of magmatic H<sub>2</sub>O-CO<sub>2</sub> fluid enriched in Mo, Au and  
650 W within an Archean sodic granodiorite stock, Mink Lake, North Western Ontario. *Econ*  
651 *Geol* 82:1931–1957

652 Büttner SH, Reid W, Glodny J, Wiedenbeck M, Chuwa G, Moloto T, Gucsik A (2016) Fluid  
653 sources in the Twangiza–Namoya Gold Belt (Democratic Republic of Congo): Evidence  
654 from tourmaline and fluid compositions, and from boron and Rb–Sr isotope systematics.  
655 *Precambrian Res* 280:161-178

656 Byerly GR, Palmer MR (1991) Tourmaline mineralization in the Barberton greenstone belt,  
657 South Africa: early Archean metasomatism by evaporite-derived boron. *Contrib Mineral*  
658 *Petr* 107:387-402

659 Castaing C, Bila M, Milési JP, Thiéblemont D, Le Metour J, Egal E, Zunimo C (2003) Notice  
660 explicative de la carte géologique et minière du Burkina Faso à 1/1 000 000 (3<sup>ème</sup> ed)

661 Catanzaro E, Champion C, Garner E, Marinenko G, Sappenfield K, Shields W (1970) Boric  
662 acid: isotopic and assay standard reference materials. National Bureau of Standards (US)  
663 *Special Publications* 260-17:1-71

664 Davis J, Miller J, Thébaud N, McCuaig C, Begg G, Jessell M, Hein K, Baratoux L (2015)  
665 Craton-scale lithostratigraphic correlation as an insight for the geodynamic evolution of  
666 the southern West African Craton. *Proceeding of the 13th Biennial SGA Meeting* 4:1587-  
667 1590

668 Dutrow BL, Henry DJ (2011) Tourmaline: a geologic DVD. *Elements* 7:301-306

669 Dutrow BL, Henry DJ (2016) Fibrous tourmaline: a sensitive probe of fluid compositions and  
670 petrologic environments. *Can Mineral* 54:311-335

671 Dutrow BL, Henry DJ (2018) Tourmaline compositions and textures: reflections of the fluid  
672 phase. *J Geosci* 63:99-110

673 Dyar MD, Wiedenbeck M, Robertson D, Cross LR, Delaney JS, Ferguson K, Francis CA, Grew  
674 ES, Guidotti CV, Hervig RL, Hughes JM, Husler J, Leeman W, McGuire AV, Rhede D,  
675 Rothe H, Paul RL, Richards I, Yates M (2001) Reference minerals for the microanalysis  
676 of light elements. *Geostand Newslett* 25:441-463

677 Egal E, Thiéblemont D, Lahondère D, Guerrot C, Costea CA, Iliescu D, Delor C, Goujou JC,  
678 Lafon JM, Tegye M (2002) Late Eburnean granitization and tectonics along the western  
679 and northwestern margin of the Archean Kénéma–Man domain (Guinea, West African  
680 Craton). *Precambrian Res* 117:57-84

681 Eglinger A, Thébaud N, Zeh A, Davis J, Miller J, Parra-Avila LA, Loucks R, McCuaig C,  
682 Belousova E (2017) New insights into the crustal growth of the Paleoproterozoic margin  
683 of the Archean Kéména-Man domain, West African craton (Guinea): Implications for  
684 gold mineral system. *Precambrian Res* 292:258-289

685 Feybesse JL, Milési JP (1994) The Archaean/Proterozoic contact zone in West Africa: a  
686 mountain belt of décollement thrusting and folding on a continental margin related to 2.1  
687 Ga convergence of Archaean cratons? *Precambrian Res* 69:199-227

688 Feybesse JL, Billa M, Guerrot C, Duguey E, Lescuyer JL, Milési JP, Bouchot V (2006) The  
689 paleoproterozoic Ghanaian province: Geodynamic model and ore controls, including  
690 regional stress modeling. *Precambrian Res* 149:149-196

691 Fontaine A, Eglinger A, Ada K, André-Mayer AS, Reisberg L, Siebenaller L, Le Mignot E,  
692 Ganne J, Poujol M (2017) Geology of the world-class Kiaka polyphase gold deposit, West  
693 African Craton, Burkina Faso. *J Afr Earth Sci* 126:96-122

694 Fougereuse D, Micklethwaite S, Ulrich S, Miller J, Godel B, Adams DT, McCuaig TC (2017)  
695 Evidence for two stages of mineralization in West Africa’s largest gold deposit: Obuasi,  
696 Ghana. *Econ Geology* 112:3-22

697 Frei R, Pettke T (1996) Mono-sample Pb-Pb dating of pyrrhotite and tourmaline: Proterozoic  
698 vs. Archean intracratonic gold mineralization in Zimbabwe. *Geology* 24:823-826

699 Fusswinkel T, Wagner T, Sakellaris G (2017) Fluid evolution of the Neoproterozoic Pampalo  
700 orogenic gold deposit (E Finland): Constraints from LA-ICPMS fluid inclusion  
701 microanalysis. *Chem Geol* 450:96-121

702 Ganne J, De Andrade V, Weinberg RF, Vidal O, Dubacq B, Kagambega N, Naba S, Baratoux  
703 L, Jessell M, Allibon J (2012) Modern-style plate subduction preserved in the  
704 Palaeoproterozoic West African craton. *Nat Geosci* 5:60-65

705 Goldfarb R, Baker T, Dubé B, Groves DI, Hart CJR, Gosselin P (2005) Distribution, character  
706 and genesis of gold deposits in metamorphic terranes. In: Hedenquist JW, Thompson  
707 JFH, Goldfarb RG, Richards JP (eds) *Economic geology 100<sup>th</sup> Anniversary volume*, Soc  
708 Econ Geol, Littleton, Colorado, USA, pp 407-450

709 Goldfarb RJ, Groves DI (2015) Orogenic gold: Common or evolving fluid and metal sources  
710 through time. *Lithos* 233:2-26

711 Goldfarb RJ, André-Mayer AS, Jowitt SM, Mudd GM (2017) West Africa: The World's  
712 Premier Paleoproterozoic Gold Province. *Econ Geol* 112:123-143

713 Grenholm M, Jessell M, Thébaud N (2019) Paleoproterozoic volcano-sedimentary series in the  
714 ca. 2.27–1.96 Ga Birimian Orogen of the southeastern West African Craton. *Precambrian*  
715 *Res* 328:161-192

716 Groves DI, Santosh M, Deng J, Wang Q, Yang L, Zhang L (2019) A holistic model for the  
717 origin of orogenic gold deposits and its implications for exploration. *Miner Deposita*  
718 55:275-292

719 Harlaux M, Mercadier J, Marignac C, Villeneuve J, Mouthier B, Cuney M (2019) Origin of the  
720 atypical Puy-les-Vignes W breccia pipe (Massif Central, France) constrained by trace  
721 element and boron isotopic composition of tourmaline. *Ore Geol Rev* 114:103132

- 722 Hazarika P, Mishra B, Pruseth KL (2015) Diverse Tourmaline Compositions from Orogenic  
723 Gold Deposits in the Hutti-Maski Greenstone Belt, India: Implications for Sources of  
724 Ore-Forming Fluids. *Econ Geol* 110:337-353
- 725 Hazarika P, Mishra B, Pruseth KL (2016) Scheelite, apatite, calcite and tourmaline  
726 compositions from the late Archean Hutti orogenic gold deposit: Implications for  
727 analogous two stage ore fluids. *Ore Geol Rev* 72:989-1003
- 728 Henry DJ, Guidotti CV (1985) Tourmaline as a petrogenetic indicator mineral: an example from  
729 the staurolite-grade metapelite of NW Maine. *Am Mineral* 70:1-15
- 730 Henry DJ, Dutrow BL (1996) Metamorphic tourmaline and its petrologic applications. In: Grew  
731 ES, Anovitz LM (eds) *Boron, Mineralogy, Petrology and Geochemistry*. *Rev Mineral*  
732 33:503-557
- 733 Henry DJ, Novak M, Hawthorne FC, Ertl A, Dutrow BL, Uher P, Pezzotta F (2011)  
734 Nomenclature of the tourmaline-supergroup minerals. *Am Mineral* 96:895-913
- 735 Hottin g, Ouédraogo OF (1976) Carte géologique de la République de Haute-Volta. Direction  
736 de la Géologie et des Mines Ouagadougou 58p
- 737 Jiang SY (1998) Stable and radiogenic isotope studies of tourmaline: an overview. *J Czech*  
738 *Geol Soc* 43:1-2
- 739 Jiang SY, Palmer MR, Yeats CJ (2002) Chemical and boron isotopic compositions of  
740 tourmaline from the Archean Big Bell and Mount Gibson gold deposits, Murchison  
741 Province, Yilgarn Craton, Western Australia. *Chem Geol* 188:229-247
- 742 Kalliomäki H, Wagner T, Fusswinkel T, Sakellaris G (2017) Major and trace element  
743 geochemistry of tourmalines from Archean orogenic gold deposits: Proxies for the origin  
744 of gold mineralizing fluids? *Ore Geol Rev* 91:906-927



745 Kawakami T, Ikeda T (2003) Boron in metapelites controlled by the breakdown of tourmaline  
746 and retrograde formation of borosilicates in the Yanai area, Ryoke metamorphic belt, SW  
747 Japan. *Contrib Mineral Petr* 145:131-150

748 King RW, Kerrich RW (1989) Strontium isotope compositions of tourmaline from lode gold  
749 deposits of the Archean Abitibi Greenstone belt (Ontario-Quebec, Canada): Implications  
750 for source reservoirs. *Chem Geol* 79:225-240

751 Kotzer TG, Kyser TK, King RW, Kerrich R (1993) An empirical oxygen- and hydrogen-isotope  
752 geothermometer for quartz-tourmaline and tourmaline-water. *Geochim Cosmochim Ac*  
753 57:3421-3426

754 Krienitz MS, Trumbull R, Hellmann A, Kolb J, Meyer F, Wiedenbeck M (2008) Hydrothermal  
755 gold mineralization at the Hira Buddini gold mine, India: constraints on fluid evolution  
756 and fluid sources from boron isotopic compositions of tourmaline. *Miner Deposita*  
757 43:421-434

758 Labou I, Benoit M, Baratoux L, Grégoire M, Ndiaye PM, Thebaud N, Béziat D, Debat P (2020)  
759 Petrological and geochemical study of Birimian ultramafic rocks within the West African  
760 Craton: Insights from Mako (Senegal) and Loraboué (Burkina Faso)  
761 lherzolite/harzburgite/wehrlite associations. *J Afr Earth Sci* 162:103677

762 Lambert-Smith JS, Rocholl A, Treloar PJ, Lawrence DM (2016) Discriminating fluid source regions in  
763 orogenic gold deposits using B-isotopes. *Geochim Cosmochim Ac* 194:57-76

764 Le Mignot E, Reisberg L, André-Mayer AS, Bourassa Y, Fontaine A, Miller J (2017) Re-Os  
765 Geochronological Evidence for Multiple Paleoproterozoic Gold Events at the Scale of the  
766 West African Craton. *Econ Geol* 112:145-168

767 Leeman W P, Sisson VB (1996) Geochemistry of boron and its implications for crustal and  
768 mantle processes. In: Grew ES, Anovitz LM (eds) *Boron, Mineralogy, Petrology and*  
769 *Geochemistry*. *Rev Mineral* 33:645-707

770 Leeman WP, Tonarini S (2001) Boron isotopic analysis of proposed borosilicate mineral  
771 reference samples. *Geostand Newslett* 25:399-403

772 Lemarchand D, Cividini D, Turpault MP, Chabaux F (2012) Boron isotopes in different grain  
773 size fractions: Exploring past and present water-rock interactions from two soil profiles  
774 (Strengbach, Vosges Mountains). *Geochim Cosmochim Acta* 98:78-93

775 London D (2011) Experimental synthesis and stability of tourmaline: a historical overview. *Can*  
776 *Mineral* 49:117-136

777 Markwitz V, Hein KAA, Miller J (2016) Compilation of West African mineral deposits: spatial  
778 distribution and mineral endowment. *Precambrian Res* 274:61-81

779 Marschall HR (2018) Boron isotopes in the ocean floor realm and the mantle. In Marschall H,  
780 Foster G (eds) *Boron Isotopes: The Fifth Element. Advances in Isotope Geochemistry*,  
781 Springer-Verlag, pp 189-215

782 Marschall HR, Jiang SY (2011) Tourmaline Isotopes: No Element Left Behind. *Elements*  
783 7:313-319

784 Marschall HR, Meyer C, Wunder B, Ludwig T, Heinrich W (2009) Experimental boron isotope  
785 fractionation between tourmaline and fluid: confirmation from in situ analyses by  
786 secondary ion mass spectrometry and from Rayleigh fractionation modelling. *Contrib*  
787 *Miner Petrol* 158:675–681

788 Masurel Q, Thébaud N, Miller J, Ulrich S, Hein KAA, Cameron G, Béziat D, Bruguier O, Davis  
789 JA (2017) Sadiola Hill: A World-Class Carbonate-Hosted Gold Deposit in Mali, West  
790 Africa. *Econ Geol* 112:23-47

791 Masurel Q, Eglinger A, Thébaud N, Allibone A, André-Mayer AS, McFarlane H, Miller J,  
792 Jessell M, Aillères L, Vanderhaeghe O, Salvi S, Baratoux L, Perrouy S, Begg G,  
793 Fougereuse D, Hayman P, Ousmane W, Tshibubudze A, Parra-Avila L, Kouamelan A,  
794 Ofori P (submitted) Gold metallogeny of the Paleoproterozoic part of the southern

795 West African Craton: capturing distinct pulses within a Paleoproterozoic orogenic cycle.  
796 Miner Deposita

797 McFarlane HB, Ailleres L, Betts P, Ganne J, Baratoux L, Jessel MW, Block S (2019) Episodic  
798 collisional orogenesis and lower crust exhumation during the Palaeoproterozoic Eburnean  
799 Orogeny: Evidence from the Sefwi Greenstone Belt, West African Craton. *Precambrian*  
800 *Res*: 325:88-110

801 McFarlane CRM, Mavrogenes J, Lentz D, King K, Allibone A, Holcombe R (2011) *Geology*  
802 and Intrusion-Related Affinity of the Morila Gold Mine, Southeast Mali. *Econ Geol*  
803 106(5):727-750

804 Meyer C, Wunder B, Meixner A, Romer RL, Heinrich W (2008) Boron-isotope fractionation  
805 between tourmaline and fluid: an experimental re-investigation. *Contrib Mineral Petr*  
806 156:259-267

807 Milesi JP, Feybesse JL, Pinna P, Deschamps Y, Kampunzu H, Muhongo S, Lescuyer JL, Le  
808 Goff E, Delor C, Billa M, Ralay F, Henry C (2004) Geological map of Africa  
809 1:10,000,000. SIGAfrique project. In: 20<sup>th</sup> Conference of African Geology. BRGM,  
810 Orléans, France, 2-7 June

811 Molnár F, Mänttári I, O'Brien H, Lahaye Y, Pakkanen L, Johanson B, Käpyaho A, Sorjonen-  
812 Ward P, Whitehouse M, Sakellaris G (2016) Boron, sulphur and copper isotope  
813 systematics in the orogenic gold deposits of the Archaean Hattu schist belt, eastern  
814 Finland. *Ore Geol Rev* 77:133-162

815 Moran AE, Sisson VB, Leeman WP (1992) Boron depletion during progressive metamorphism:  
816 implications for subduction processes. *Earth Planet Sc Lett* 111:331–349

817 Morgan GB, London D (1989) Experimental reactions of amphibolite with boron-bearing  
818 aqueous fluids at 200 Mpa: implications for tourmaline stability and partial melting in  
819 mafic rocks. *Contrib Mineral Petr* 102:281-297

820 Mueller AG, de Laeter JR, Groves DI (1991) Strontium isotope systematics of hydrothermal  
821 minerals from epigenetic Archean gold deposits in the Yilgarn Block, Western Australia.  
822 Econ Geol 86:780-809

823 Naba S, Lompo M, Debat P, Bouchez JL, Béziat D (2004) Structure and emplacement model  
824 for late-orogenic Paleoproterozoic granitoids: the Tenkodogo-Yamba elongate pluton  
825 (Eastern Burkina Faso). J Afr Earth Sci 38:41-57

826 Nakano T, Nakamura E (2001) Boron isotope geochemistry of metasedimentary rocks and  
827 tourmalines in a subduction zone metamorphic suite. Phy Earth Planet In 127:233-252

828 Parra-Avila LA, Kemp AIS, Fiorentini ML, Belousova E, Baratoux L, Block S, Jessell M,  
829 Bruguier O, Begg GC, Miller J, Davis J, McCuaig TC (2017) The geochronological  
830 evolution of the Paleoproterozoic Baoulé-Mossi domain of the Southern West African  
831 Craton. Precambrian Res 300:1-27

832 Parra-Avila LA, Baratoux L, Eglinger A, Fiorentini ML, Block S (2019) The Eburnean  
833 magmatic evolution across the Baoulé-Mossi domain: Geodynamic implications for the  
834 West African Craton. Precambrian Res 332 [105392]

835 Perrouty S, Aillères L, Jessell MW, Baratoux L, Bourassa Y, Crawford B (2012) Revised  
836 Eburnean geodynamic evolution of the gold-rich southern Ashanti Belt, Ghana, with new  
837 field and geophysical evidence of pre-Tarkwaian deformations. Precambrian Res 204-  
838 205:12-39

839 Philipps GN, Powell R (2010) Formation of gold deposits: a metamorphic devolatilization  
840 model. J Metam Geol 28:689-718

841 Pouclet A, Doumbia S, Vidal M (2006) Geodynamic setting of the Birimian volcanism in  
842 central Ivory Coast (western Africa) and its place in the Palaeoproterozoic evolution of  
843 the Man Shield. B Soc Geol Fr 177:105-121

844 Robertson M, Peters L (2016) West African goldfields. Episodes 39:155-176

845 Rogers AJ, Kolb J, Meyer FM, Vennemann T (2013) Two stages of gold mineralization at Hutti  
846 mine. *Miner Deposita* 48:99-114

847 Roux P, Lemarchand D, Hughes HJ, Turpault MP (2015) A Rapid Method for Determining  
848 Boron Concentration (ID-ICP-MS) and  $\delta^{11}\text{B}$  (MC-ICP-MS) in Vegetation Samples after  
849 Microwave Digestion and Cation Exchange Chemical Purification. *Geostand Newslett*  
850 39:453-466

851 Rowins SM, Groves DI, McNaughton NJ, Palmer MR, CS Eldridge (1997) A reinterpretation  
852 of the role of granitoids in the genesis of Neoproterozoic gold mineralization in the Telfer  
853 Dome, Western Australia. *Econ Geol* 92:133-160

854 Sciuba M, Beaudoin G, Makvandi S (2020) Chemical composition of tourmaline in orogenic  
855 gold deposits. *Miner Dep* in press

856 Slack JF (1996) Tourmaline associations with hydrothermal ore deposits. In: Grew ES, Anovitz  
857 LM (eds) *Boron, Mineralogy, Petrology and Geochemistry*. *Rev Mineral* 33:559-643

858 Slack JF, Trumbull RB (2011) Tourmaline as a Recorder of Ore-Forming Processes. *Elements*  
859 7:321-326

860 Spear FS, Kohn MJ, Cheney JT (1999) P-T paths from anatexis pelites. *Contrib Mineral Petr*,  
861 134:17-32

862 Thébaud N, Allibone A, Masurel Q, Eglinger A, Davis J, André-Mayer AS, Miller J, Jessell M  
863 The Paleoproterozoic (Rhyacian) gold deposits of West Africa (2020, accepted, proof in  
864 progress) *Econ Geology*

865 Thompson AB (1982) Dehydration melting of pelitic rocks and the generation of H<sub>2</sub>O-  
866 undersaturated granitic liquids. *Am J Sci* 282:1567-1595

867 Tomkins AG (2013) On the source of orogenic gold. *Geology* 41:1255-1256

868 Trumbull RB, Slack JF (2018) Boron isotopes in the continental crust: granites, pegmatites,  
869 felsic volcanic rocks, and related ore deposits. In: Marschall HR, Foster GL (Eds), *Boron*

870 Isotopes – The Fifth Element. Advances in Isotope Geochemistry, Springer-Verlag, pp  
871 249-272

872 Tshibubudze A, Hein KAA (2013) Structural setting of gold deposits in the Oudalan-Gorouol  
873 volcano-sedimentary belt east of the Markoye Shear Zone, West African Craton. J Afr  
874 Earth Sci 80:31-47

875 Tshibubudze A, Hein KAA, Marquis P (2009) The Markoye Shear Zone in NE Burkina Faso.  
876 J Afr Earth Sci 55:245-256

877 van Hinsberg VJ, Henry DJ, Marschall HR (2011) Tourmaline: an ideal indicator of its host  
878 environment. Can Mineral 49:1-16

879 Vegas N, Naba S, Bouchez JL, Jessell M (2008) Structure and emplacement of granite plutons  
880 in the Paleoproterozoic crust of Eastern Burkina Faso: rheological implications. Int J  
881 Earth Sci 97:1165-1180

882 Vielzeuf D, Holloway JR (1988) Experimental determination of the fluid-absent melting  
883 relations in the pelitic system. Contrib Mineral Petr 98:257-276

884 von Goerne G, Franz G, Heinrich W (2001) Synthesis of tourmaline solid solutions in the  
885 system  $\text{Na}_2\text{O-MgO-Al}_2\text{O}_3\text{-SiO}_2\text{-B}_2\text{O}_3\text{-H}_2\text{O-HCl}$  and the distribution of Na between  
886 tourmaline and fluid at 300 to 700°C and 200 MPa. Contrib Mineral Petr 141:160-173

887 von Goerne G, Franz G, van Hinsberg VJ (2011) Experimental determination of Na-Ca  
888 distribution between tourmaline and fluid in the system  $\text{CaO-Na}_2\text{O-MgO-Al}_2\text{O}_3\text{-SiO}_2\text{-}$   
889  $\text{B}_2\text{O}_3\text{-H}_2\text{O}$ . Can Mineral 49:137-152

890 Vry J, Powell R, Golden KM, Petersen K (2010) The role of exhumation in metamorphic  
891 dehydration and fluid production. Nat Geosci 3:31-35

892 Wang LG, McNaughton NJ, Groves DI (1993) An overview of the relationship between  
893 granitoid intrusions and gold mineralization in the Archaean Murchison Province,  
894 Western Australia. Miner Deposita 28:482-494

895 Wunder B, Meixner A, Romer RL, Wirth R, Heinrich W (2005) The geochemical cycle of  
896 boron: constraints from boron isotope partitioning experiments between mica and fluid.  
897 Lithos 84:206-216

898 Wyman D, Kerrich R (1988) Alkaline magmatism, major structures, and gold deposits:  
899 implications for greenstone belt gold metallogeny. Econ Geol 83:454-461

900 Xue Y, Campbell IH, Ireland TR, Holden P, Armstrong R (2013) No mass-independent sulfur  
901 isotope fractionation in auriferous fluids supports a magmatic origin for Archean gold  
902 deposits. Geology 41:791-794

903 Yavuz F, Karakaya N, Yildirim DK, Karakaya MC (2014) A Windows program for calculation  
904 and classification of tourmaline-supergroup (IMA-2011). Comput Geosci 63:70-87  
905

906 **Figure captions**

907

908 **Figure 1. A.** Location and geological setting of the Kiaka orogenic gold deposit in the West  
909 African Craton (modified after Castaing et al. 2003; Naba et al. 2004; Milési et al. 2004; Vegas  
910 et al. 2008; Ganne et al. 2012). The Kénéma Man domain (Archean nucleus) and the Baoulé-  
911 Mossi domain (Paleoproterozoic juvenile crust) form two domains separated by the Sassandra  
912 Fault (SF). Volcano-sedimentary belts include Banfora (BA), Houndé (HO), Boromo (BO),  
913 Lawra (LW), Goren (GO), Bui (BU), Ashanti (AS) and Sefwi (SW), Haute Comoé basin (HC),  
914 and Manga Fada-N’Gourma belt (MFG). These belts are separated into dark green for mafic  
915 volcanics rocks and light green for volcano-sedimentary rocks and intermediate to felsic  
916 igneous rocks (Baratoux et al. 2011). A spatial association is found between gold deposits of  
917 the Baoulé-Mossi domain and major tectonic structures such as the Grenville-Ferkessedougou-  
918 Bobo-Dialouso (GFBF), Ouango-Fitini (OF) and Markoye (MSZ; this study) shear zones. For  
919 interpretation of the colors, the reader is referred to the web version of this article. **B.** Geology  
920 of the Manga Fada-N’Gourma greenstone belt with MSZ (thick black lines) and location of the  
921 Kiaka gold deposit (Fontaine et al. 2017). **C.** Local geology of the Kiaka deposit showing the  
922 location of the drillholes and cross-sections. Mineralized envelopes are projected at surface  
923 from drillhole data (modified from Fontaine et al. 2017). **D.** NW-striking section 6100 showing  
924 the location of the diorite plug.

925

926 **Figure 2.** Paragenetic sequence of the Kiaka gold deposit and relationships with the structural  
927 events and hydrothermal alteration.

928

929 **Figure 3.** Mineralogical and textural features of tourmaline in the alteration zones of the Kiaka  
930 gold deposit. **A & B.** Muscovite schist containing folded garnet-biotite-chlorite-muscovite layer



931 with detrital tourmaline (*Tur<sub>1</sub>*) (sample KDH75-64.9). **C & D.** Metagreywacke composed of  
932 quartz, plagioclase, and biotite, containing disseminated tourmaline and clinozoisite (sample  
933 KDH29-311.8). **E & F.** Metamafic rock-hosted tourmaline porphyroblasts (*Tur<sub>2</sub>*) associated  
934 with D<sub>2K<sub>i</sub></sub> biotite-clinozoisite-titanite-pyrrhotite alteration assemblage and crosscut by chlorite  
935 (Chl 3)-calcite D<sub>4K<sub>i</sub></sub> veinlet (sample KDH291-56.2). Mineral abbreviations: Bt=biotite,  
936 Cal=calcite, Chl=chlorite, Czo=clinozoisite, Kfs=K-feldspar, Grt=garnet, Ms=moscovite,  
937 Qtz=quartz, Pl=plagioclase, Po=pyrrhotite, Ttn=titanite, Tur=tourmaline.

938

939 **Figure 4.** Petrography of hydrothermal tourmaline (*Tur<sub>2</sub>*) hosted in metagreywacke (sample  
940 KDH29-311.8). **A.** Backscattered electron images of euhedral grains of hydrothermal  
941 tourmaline in an assemblage of quartz, biotite, K-feldspar, and pyrrhotite. Note the  
942 homogeneity of the tourmaline grains. **B.** Plane-polarized transmitted-light photomicrograph of  
943 hydrothermal tourmaline grains.

944

945 **Figure 5.** Petrography of metamafic rock-hosted hydrothermal tourmaline (*Tur<sub>2</sub>*)  
946 porphyroblasts (sample KDH291-56.2). **A.** Global view of the three studied tourmaline  
947 porphyroblasts (Grain 1, Grain 2, and Grain 3) observed by plane-polarized transmitted light  
948 (x150) and **B.** interpretation sketch below (modified after Fontaine et al. 2017). The  
949 hydrothermal assemblage is cut by a D<sub>4K<sub>i</sub></sub> calcite-chlorite vein. **C.** Backscattered electron image  
950 of a tourmaline porphyroblast (Grain 2) showing complex zoning and numerous sulfide  
951 inclusions.

952

953

954 **Figure 6.** X-ray elemental maps of a poikilitic tourmaline porphyroblast (*Tur<sub>2</sub>*, Grain 2) hosted  
955 in metamafic rock (sample KDH291-56.2). **A** and **B** show the tourmaline grain in transmitted

956 light (TL) and backscattered electrons (BSE) (same as Figure 5C). Relative intensities of the  
957 elements Fe, Mg, Al, Ca, Na, and Ti (C, D, E, F, and G) are shown with count/sec. scales.

958

959 **Figure 7.** Chemical compositions of hydrothermal tourmaline (*Tur*<sub>2</sub>) hosted in metamafic rock  
960 (sample KDH291-56.2) and metagreywacke (sample KDH29-311.8). **A.** Binary diagram  
961  $X_{\text{vacancy}}/(X_{\text{vacancy}}+\text{Na})$  vs.  $\text{Mg}/(\text{Fe}+\text{Mg})$ , indicating that *Tur*<sub>2</sub> belongs to domain dravite/oxy-  
962 dravite. **B.** Binary diagram Fe vs. Mg, showing low Mg composition for metagreywacke-hosted  
963 *Tur*<sub>2</sub>, and a richer Mg content for *Tur*<sub>2</sub> hosted in metamafic volcanic rock. **C.** Binary diagram  
964  $X_{\text{vacancy}}$  vs. Al, showing a dravite-schorl composition for metamafic rock tourmaline, and a  
965 composition closer to foitite/magnesio-foitite for metagreywacke tourmaline. **D.** Binary  
966 diagram Fe vs Al, highlighting higher Al content for metagreywacke tourmaline compared to  
967 metamafic rock tourmaline. **E.** Ternary diagram Ca- $X_{\text{vacancy}}$ -(Na+K) illustrating the belonging  
968 of *Tur*<sub>2</sub>, for both lithologies, to the alkali group. **F.** Ternary diagram Al-Fe-Mg. The numbered  
969 fields in the Al-Fe-Mg diagram correspond to the compositional range of tourmaline hosted in  
970 different rock types as defined by Henry and Guidotti (1985): 1- Li-rich granitoids, pegmatites  
971 and aplites; 2- Li-poor granitoids, pegmatites and aplites; 3- Fe<sup>3+</sup>-rich quartz-tourmaline rocks  
972 (hydrothermally altered granitoids); 4- Al-rich metapelites and metapsammites; 5- Al-poor  
973 metapelites and metapsammites; 6- Fe<sup>3+</sup>-rich quartz-tourmaline rocks, calc-silicate rocks and  
974 metapelites; 7- Low-Ca meta-ultramafic rocks and Cr-V-rich metasediments; 8-  
975 Metacarbonates and metapyroxenites.

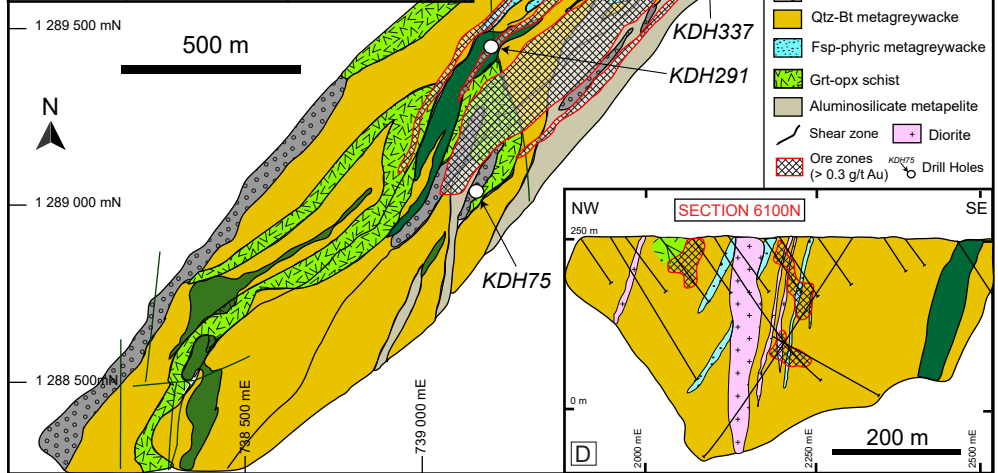
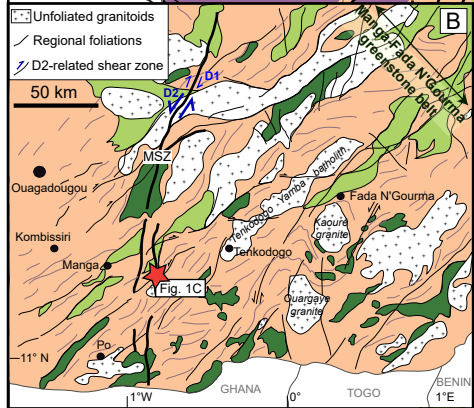
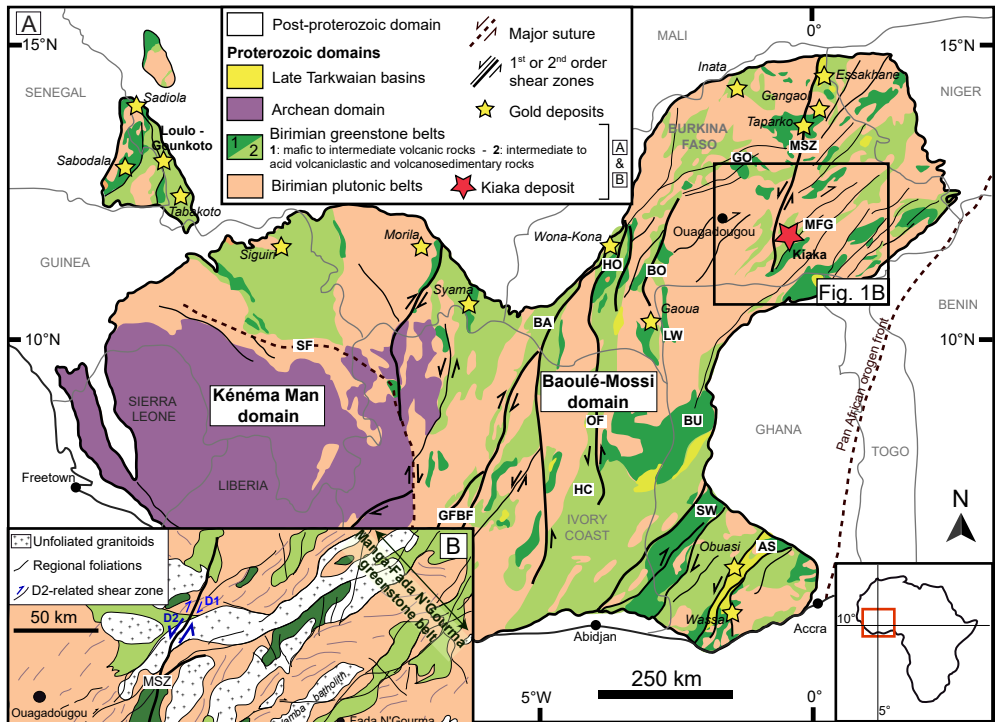
976 **Figure 8.** Boron isotope compositions of hydrothermal tourmaline (*Tur*<sub>2</sub>) from the Kiaka gold  
977 deposit. **A.** Histogram showing the  $\delta^{11}\text{B}$  distribution of tourmaline hosted in metamafic rock  
978 (sample KDH291-56.2) and metagreywacke (sample KDH29-311.8) compared to the whole-  
979 rock  $\delta^{11}\text{B}$  compositions of the diorite (sample KDH337-44.1) and the muscovite schist (sample  
980 KDH75-64.9). **B.**  $\delta^{11}\text{B}$  compositional range of tourmaline from orogenic gold deposits

981 worldwide. Data are compiled from (1) Lambert-Smith et al. (2016); (2) Molnár et al. (2016);  
982 (3) Krienitz et al. (2008); (4, 5) Jiang et al. (2002); (6) Beaudoin et al. (2013); (7, 8, 9) Baksheev  
983 et al. (2015). C.  $\delta^{11}\text{B}$  compositional range of tourmaline hosted in variable lithologies  
984 worldwide (Marschall and Jiang 2011; Trumbull and Slack 2018).

985

986

987 **Figure 9.** Boron isotope fractionation curves between tourmaline and fluid for a stepwise  
988 decreasing temperature from 650 to 350°C (after Büttner et al. 2016). The isotopic composition  
989 of fluid and tourmaline are calculated for a starting initial fluid composition of  $\delta^{11}\text{B} = -21.5\text{‰}$   
990 using the Rayleigh fractionation model of Marschall et al. (2009) and the temperature-  
991 dependent tourmaline-fluid fractionation values of Meyer et al. (2008).



Deformation	D1	SYN-D2	LATE-D2	D3	D4
<b>Metamorphism</b>	Prograde	Prograde (7.5 kbar; 550°C) Diorite emplacement and shearing		D3 <sub>K1</sub> -D4 <sub>K1</sub> events Retrograde Reactivation of D2 shearzones	
<b>Tourmaline generation</b>					
<i>Tur1</i> : Detrital Rounded, brown to blue <sup>1,2</sup> <u>with Grt, Bt and Ms</u>					
<i>Tur2</i> : Hydrothermal Euhedral brown, inclusion-poor <sup>1</sup> Poikiloblastic mm and inclusion-rich <sup>3</sup>	<u>with Ap, Qtz and Po inclusions</u>		<u>with Po, Ccp, Chl, Czo and Act inclusions</u>		
<b>Mineralization</b>					
Po ± (Py, Ccp) disseminations in Bt replacement zones ( <b>1-3 g/t Au</b> ) <sup>1</sup>	—————				
Apy ± (Lo) disseminations and Qz veinlets <sup>1</sup>	—————				
Po ± (Py) in calc-silicate hydrothermal breccia	-----				
Visible Au in Qtz-carbonate veinlets ( <b>50-60 g/t Au</b> )	—————				
<b>Alteration</b>					
Biotitization <sup>1,3</sup>	—————				
Calc-silicate alteration <sup>3</sup>	-----				
Tourmalinization <sup>1,3</sup>	—————				
Sericitization	-----				
Chloritization <sup>3</sup>	<u>Chl1</u> -----				<u>Chl2</u> ----- <u>Chl3</u> -----
Carbonatation	-----				




————— Major  
 ————— Minor  
 ----- Rare

<sup>1</sup> mainly in aluminosilicate-bearing metapelites and quartz-biotite metagreywacke

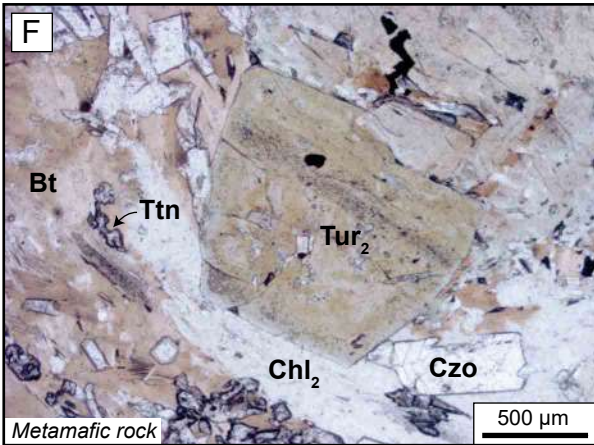
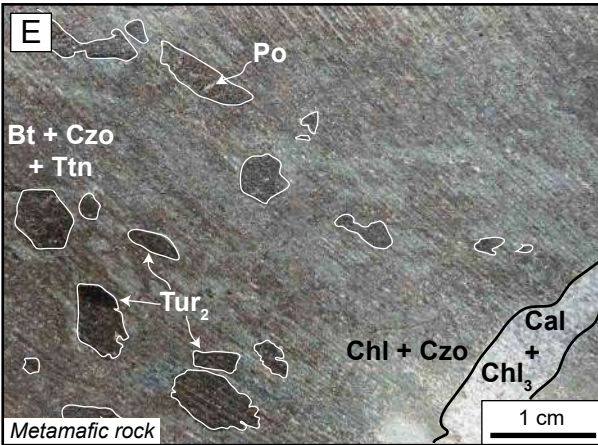
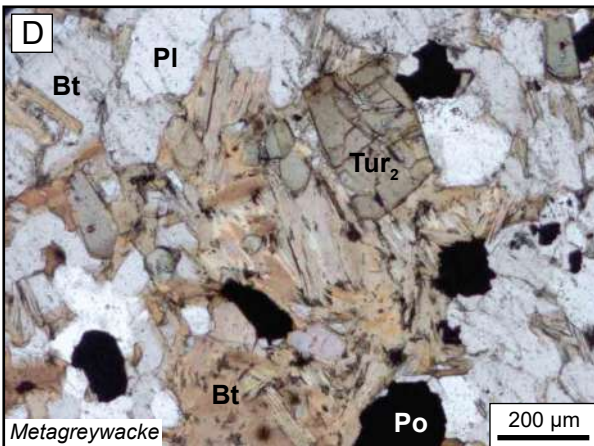
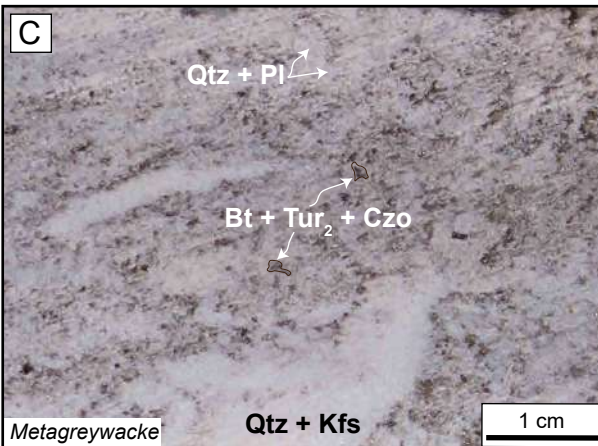
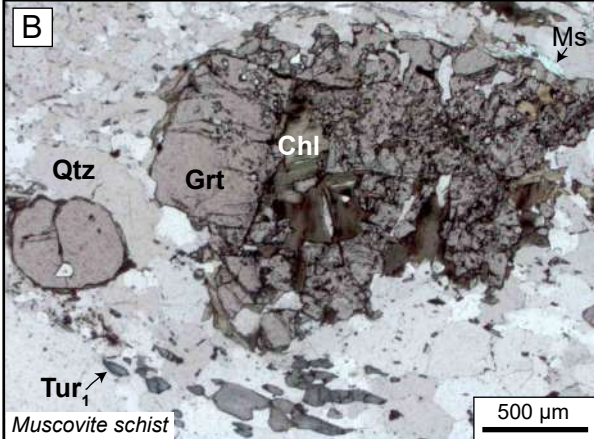
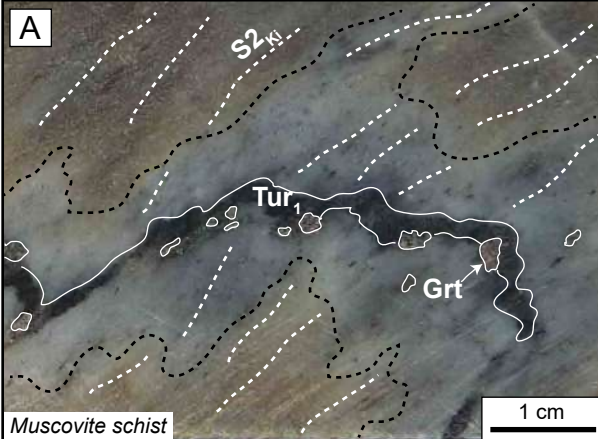
<sup>2</sup> mainly in quartz-muscovite schist

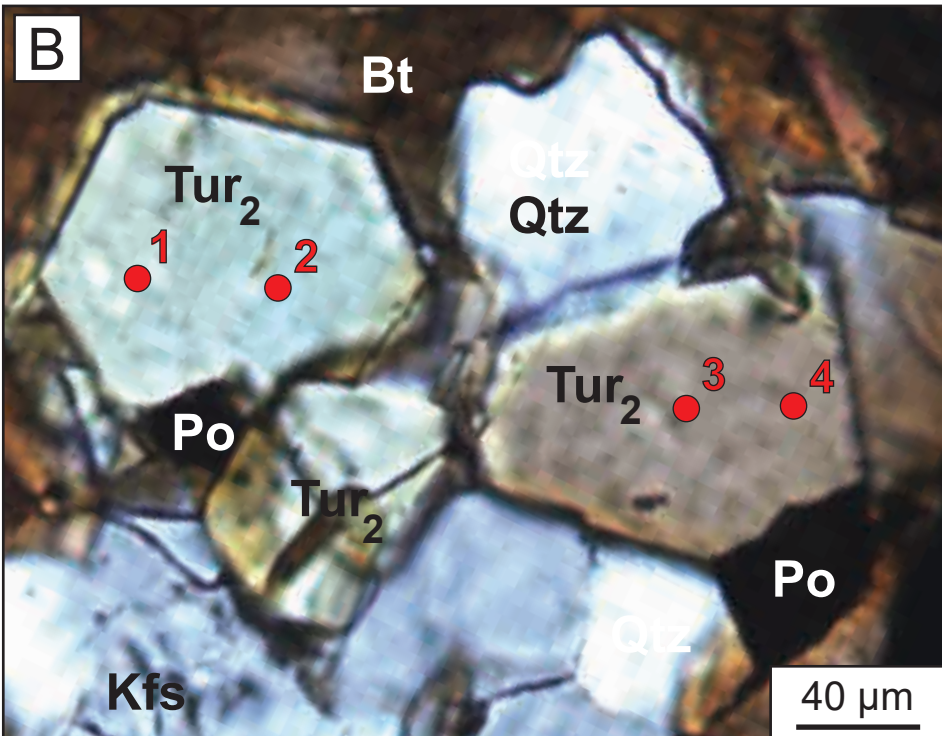
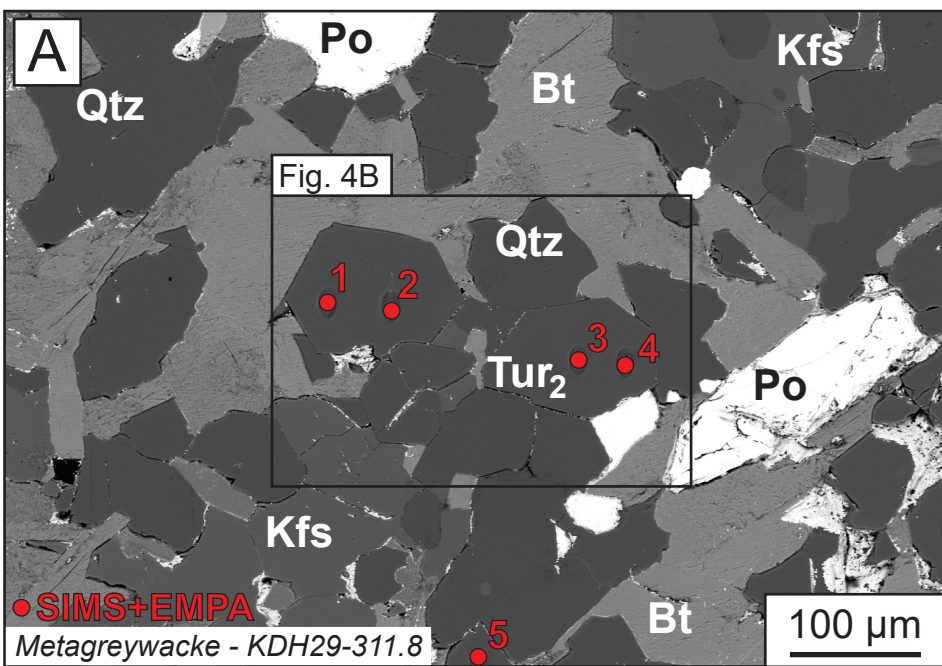
<sup>3</sup> mainly in metamafic rock

Deformation	D1	SYN-D2	LATE-D2	D3	D4
<b>Metamorphism</b>	Prograde	Prograde (7.5 kbar; 550°C) Diorite emplacement and shearing		D3 <sub>KI</sub> -D4 <sub>KI</sub> events Retrograde Reactivation of D2 shearzones	
<b>Tourmaline generation</b>					
<i>Tur</i> <sub>1</sub> : Detrital Rounded, brown to blue <sup>1,2</sup> <u>with Grt, Bt and Ms</u>					
<i>Tur</i> <sub>2</sub> : Hydrothermal Euhedral brown, inclusion-poor <sup>1</sup> Poikiloblastic mm and inclusion-rich <sup>3</sup>	<u>with Ap, Qtz and Po inclusions</u>		<u>with Po, Ccp, Chl, Czo and Act inclusions</u>		
<b>Mineralization</b>					
Po ± (Py, Ccp) disseminations in Bt replacement zones <b>(1-3 g/t Au)</b> <sup>1</sup>	—————				
Apy ± (Lo) disseminations and Qz veinlets <sup>1</sup>	—————				
Po ± (Py) in calc-silicate hydrothermal breccia	-----				
Visible Au in Qtz-carbonate veinlets <b>(50-60 g/t Au)</b>	—————				
<b>Alteration</b>					
Biotitization <sup>1,3</sup>	—————				
Calc-silicate alteration <sup>3</sup>	-----				
Tourmalinization <sup>1,3</sup>	—————				
Sericitization	-----				
Chloritization <sup>3</sup>	<u>Chl<sub>1</sub></u> -----			----- <u>Chl<sub>2</sub></u>	----- <u>Chl<sub>3</sub></u>
Carbonatation					-----

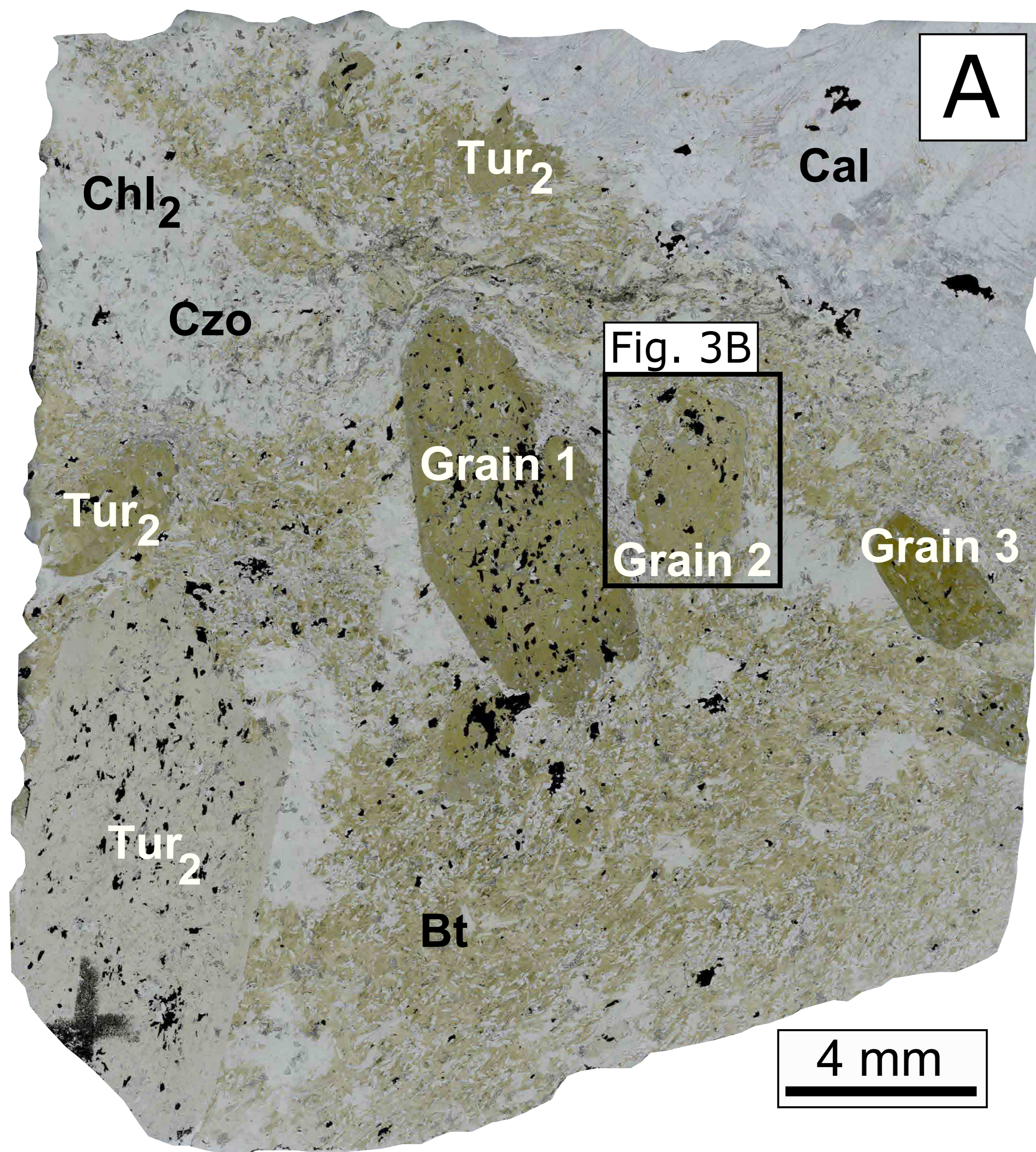
 Major  
 Minor  
 Rare

<sup>1</sup> mainly in aluminosilicate-bearing metapelites and quartz-biotite metagreywacke  
<sup>2</sup> mainly in quartz-muscovite schist  
<sup>3</sup> mainly in metamafic rock

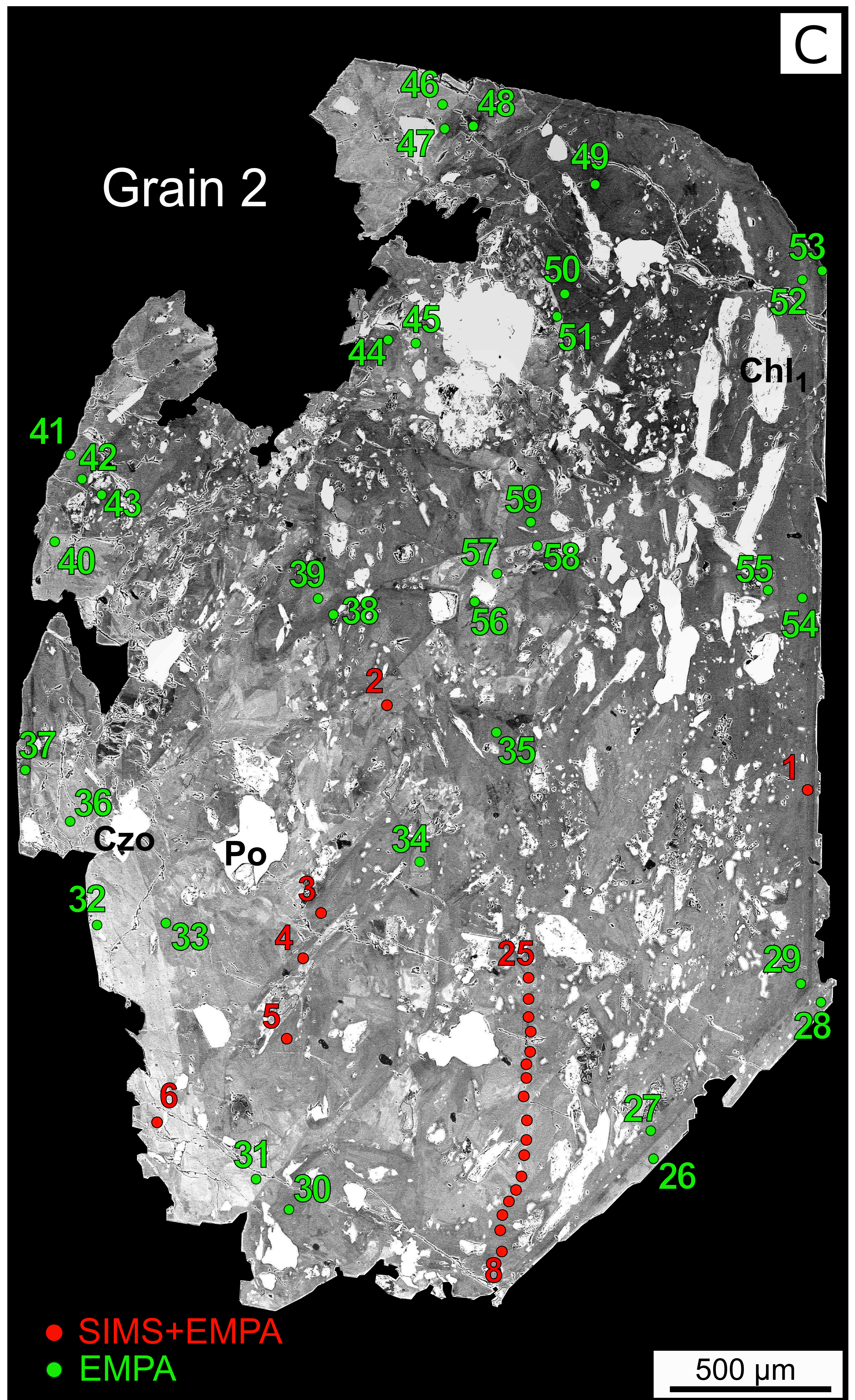
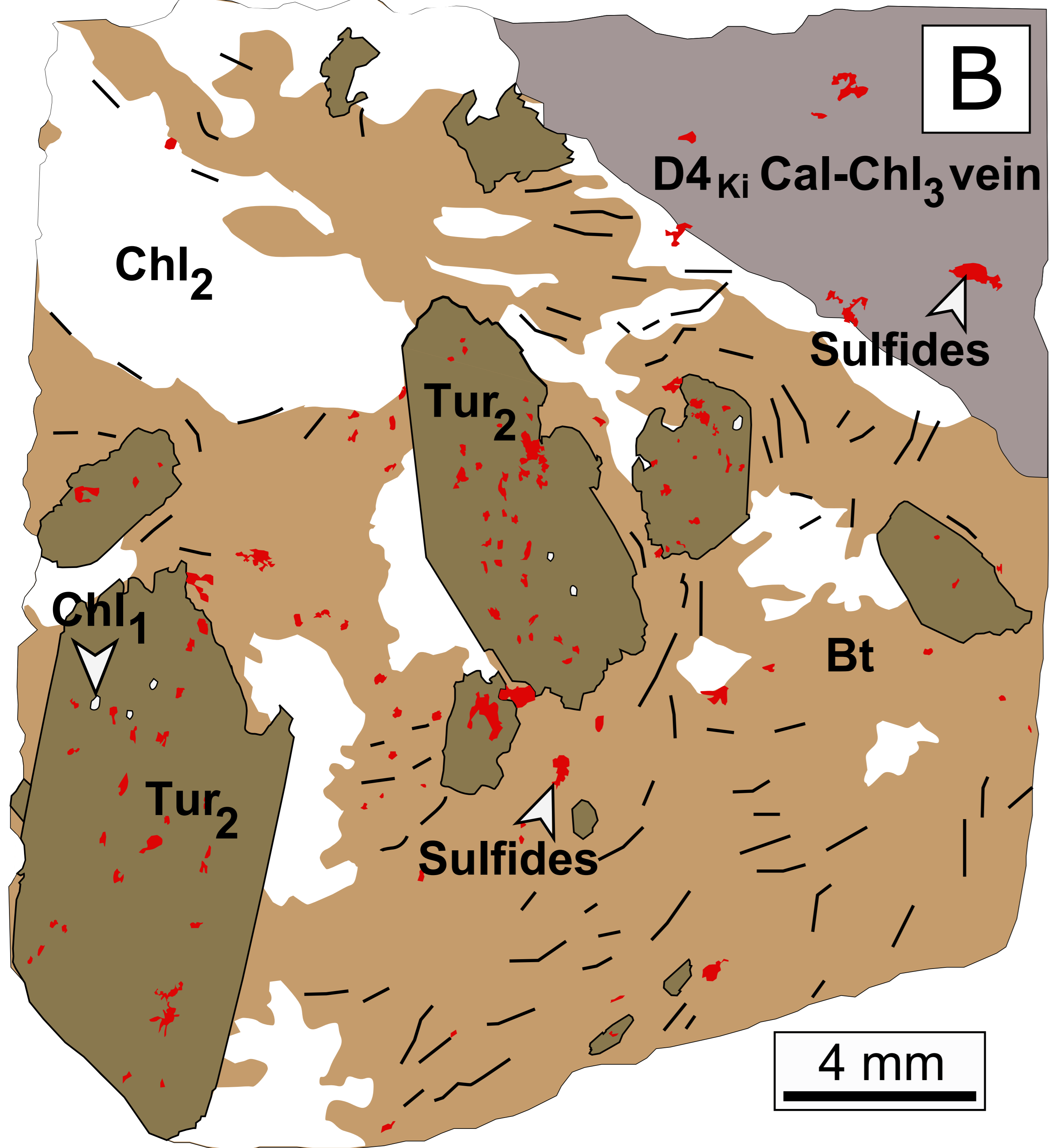


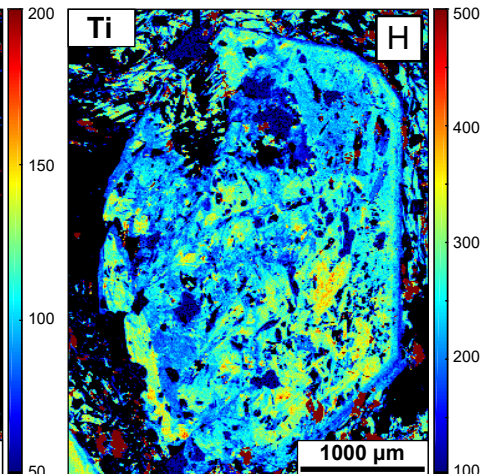
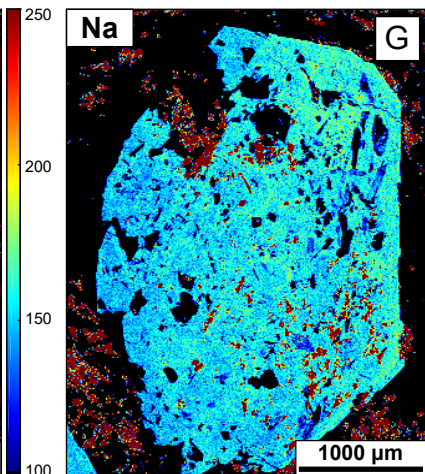
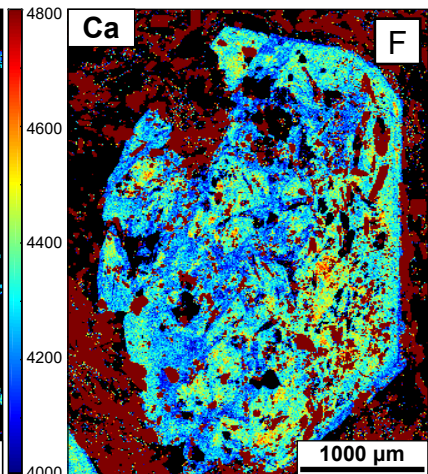
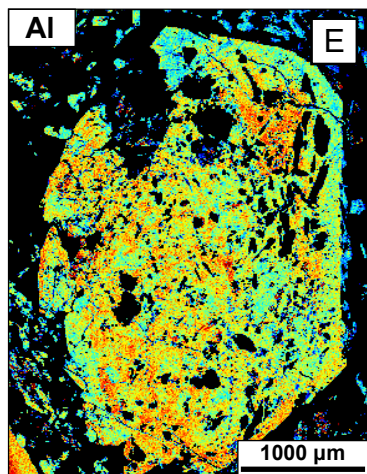
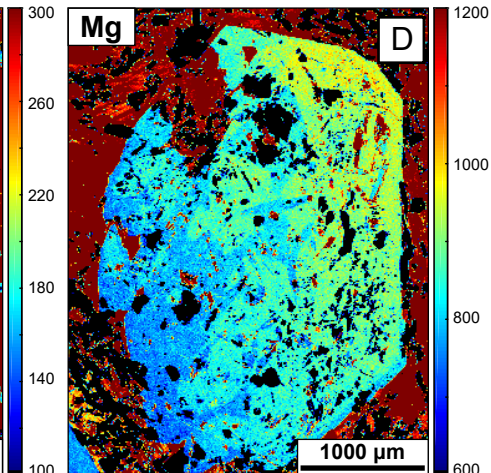
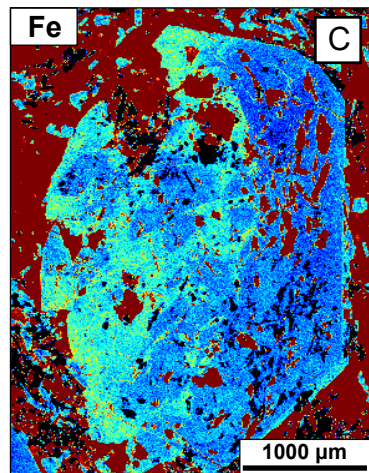
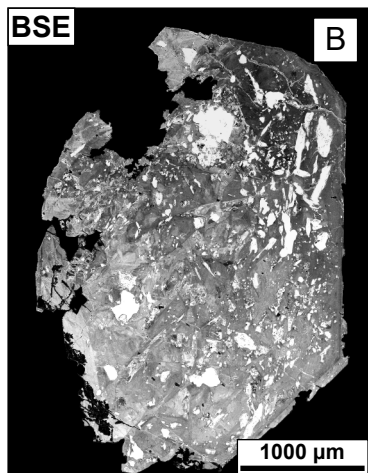
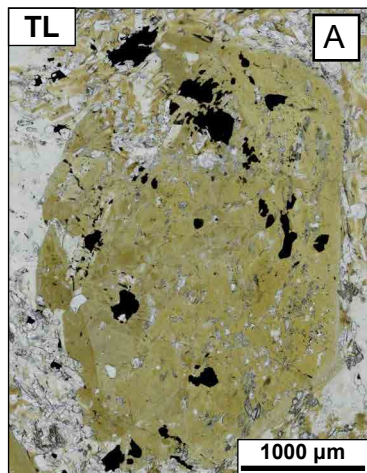


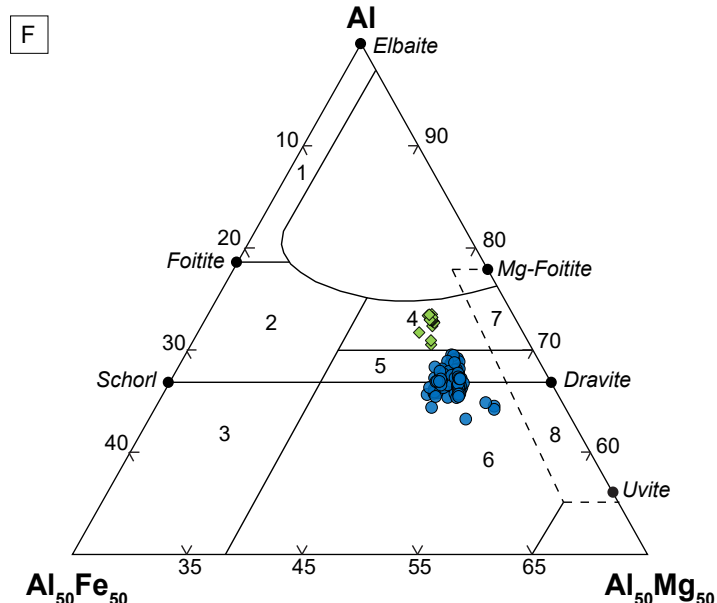
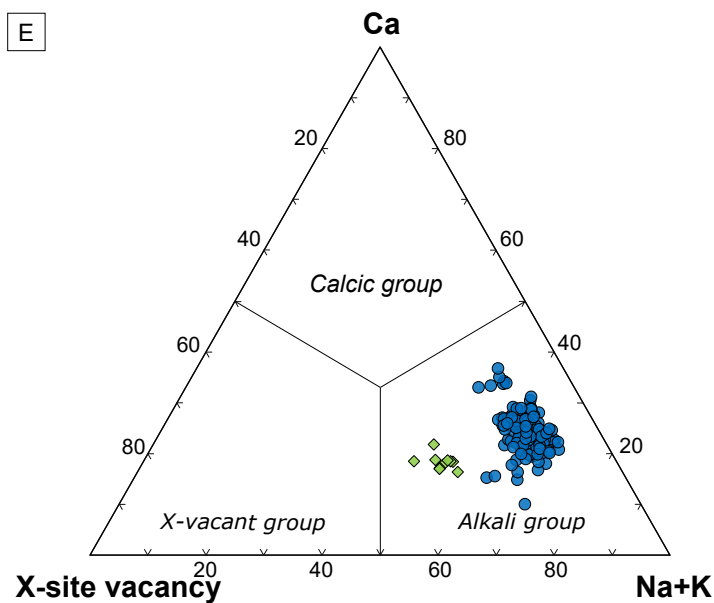
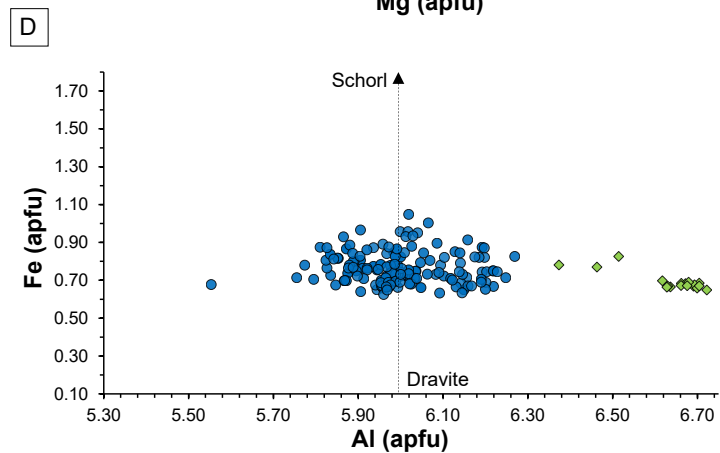
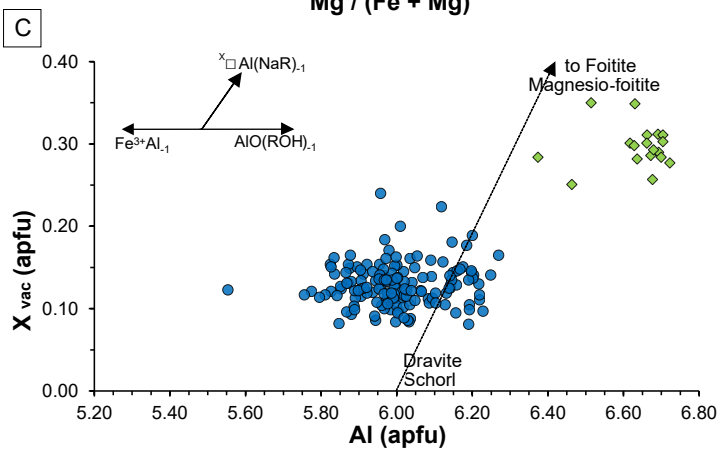
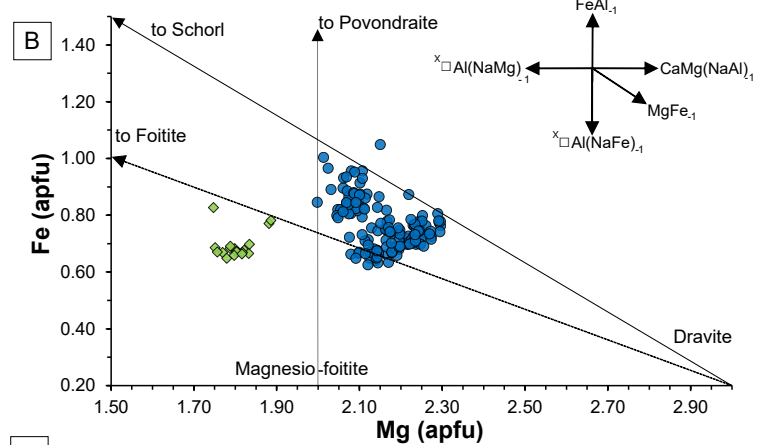
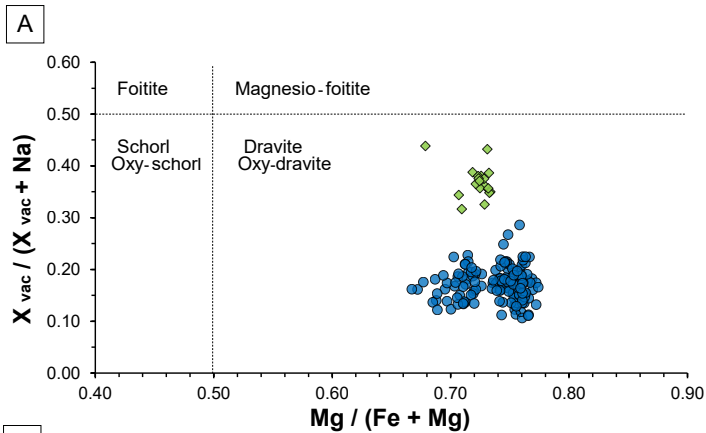




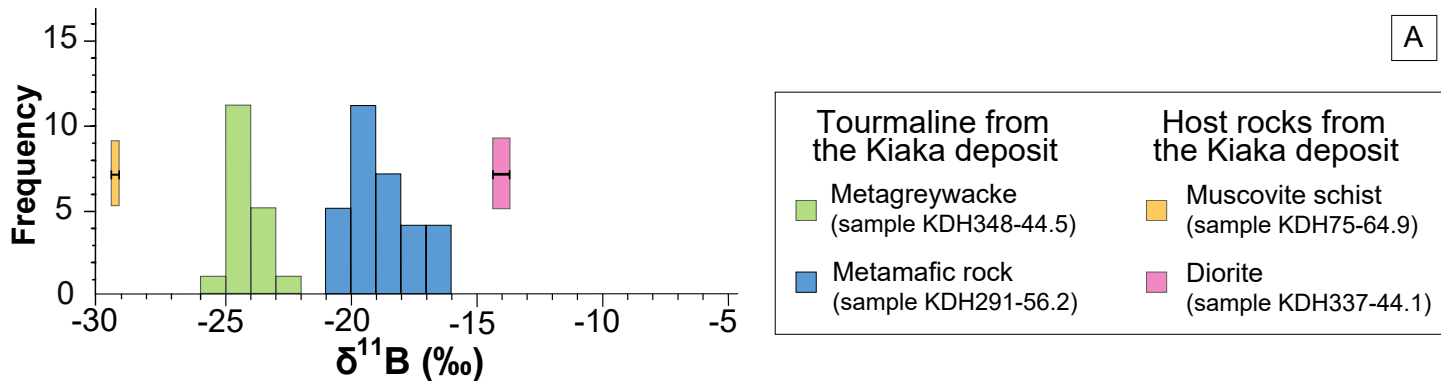
Metamafic rock - KDH291-56.2





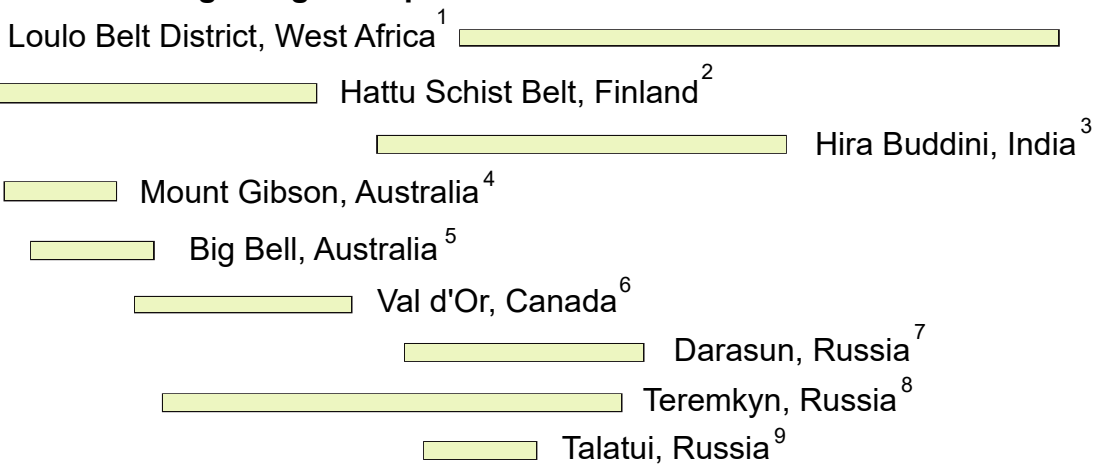


● Metamafic rock (sample KDH291-56.2)      ◆ Metagreywacke (sample KDH29-311.8)



**B**

$\delta^{11}\text{B}$  of tourmaline from orogenic gold deposits



**C**

$\delta^{11}\text{B}$  of tourmaline hosted in...

